



Spark plasma synthesis under high pressure for advanced materials

Alain Largeteau, Mythili Prakasam

► To cite this version:

Alain Largeteau, Mythili Prakasam. Spark plasma synthesis under high pressure for advanced materials. *Materials*, 14(19) : 15(14), pp.1-28, 2022. hal-03847579

HAL Id: hal-03847579

<https://hal.science/hal-03847579>

Submitted on 10 Nov 2022

HAL is a multi-disciplinary open access archive for the deposit and dissemination of scientific research documents, whether they are published or not. The documents may come from teaching and research institutions in France or abroad, or from public or private research centers.

L'archive ouverte pluridisciplinaire **HAL**, est destinée au dépôt et à la diffusion de documents scientifiques de niveau recherche, publiés ou non, émanant des établissements d'enseignement et de recherche français ou étrangers, des laboratoires publics ou privés.



Distributed under a Creative Commons Attribution - NonCommercial - NoDerivatives 4.0 International License



Spark Plasma Synthesis under High Pressure for Advanced Materials

Guest Editors:

Dr. Alain Largeteau

1. University of Bordeaux,
Bordeaux, France
2. ICMCB (UMR 5026) - CNRS,
33608 Pessac, France

alain.largeteau@icmcb.cnrs.fr

Dr. Mythili Prakasam

ICMCB (UMR 5026) - CNRS, 33608
Pessac, France

mythli.prakasam@icmcb.cnrs.fr

Deadline for manuscript
submissions:

20 January 2023

Message from the Guest Editors

Spark plasma sintering is being increasingly employed in the field of sintering to increase the level of solid chemistry reaction that induces a decrease in the sintering temperature over a shorter duration by limiting grain growth. Spark plasma synthesis focuses on a new approach in advanced materials, such as the assembly of various materials (multimaterials), the densification of composites less than their melting temperatures, the welding of metal alloys, electromigration, etc.

The application of high pressure in SPS—instead of conventional pressure which is restricted to the use of graphite molds—with other types of molds allows a new high-pressure field in materials science for refractory compositions, high-pressure phases (diamond, cubic boron nitride, etc.), phase transitions, hydro(solvo)thermal, etc., for innovative fields of application.

Combination of the spark plasma process using high-pressure tools for material synthesis will be addressed in this Special Issue.

To this end, we are pleased to invite you to submit a manuscript to this Special Issue. Full articles, papers and reviews are welcome.



Published papers (2 papers)

High Pressure (HP) in Spark Plasma Sintering (SPS) Processes: Application to the Polycrystalline Diamond

by [Jérémy Guignard](#), [Mythili Prakasam](#) and [Alain Largeteau](#)

Materials **2022**, *15*(14), 4804; <https://doi.org/10.3390/ma15144804> - 09 Jul 2022





Powder Metallurgical Processing and Characterization of Molybdenum Addition to Tungsten Heavy Alloys by Spark Plasma Sintering

by [A. Raja Annamalai](#), [A. Muthuchamy](#), [Muthe Srikanth](#), [Senthilnathan Natarajan](#), [Shashank Acharya](#), [Anup Khisti](#) and [Chun-Ping Jen](#)

Materials **2021**, *14*(19), 5756; <https://doi.org/10.3390/ma14195756> - 02 Oct 2021

Article

Powder Metallurgical Processing and Characterization of Molybdenum Addition to Tungsten Heavy Alloys by Spark Plasma Sintering

A. Raja Annamalai ¹ , A. Muthuchamy ², Muthe Srikanth ¹ , Senthilnathan Natarajan ¹ , Shashank Acharya ¹, Anup Khisti ¹ and Chun-Ping Jen ^{3,4,*} 

¹ Centre for Innovative Manufacturing Research, Vellore Institute of Technology, Vellore 632014, Tamil Nadu, India; raja.annamalai@vit.ac.in (A.R.A.); muthe.srikanth@vit.ac.in (M.S.); senthilnathan.n@vit.ac.in (S.N.); achashash99@gmail.com (S.A.); anupkhisti96@gmail.com (A.K.)

² Department of Metallurgical and Materials Engineering, NIT Tiruchirappalli, Tiruchirappalli 620015, Tamil Nadu, India; muthuchamy@nitt.edu

³ School of Dentistry, College of Dental Medicine, Kaohsiung Medical University, Kaohsiung 80708, Taiwan

⁴ Department of Mechanical Engineering, Advanced Institute of Manufacturing for High-Tech Innovations, National Chung Cheng University, Chia-Yi 62102, Taiwan

* Correspondence: chunpingjen@alum.ccu.edu.tw



Citation: Annamalai, A.R.; Muthuchamy, A.; Srikanth, M.; Natarajan, S.; Acharya, S.; Khisti, A.; Jen, C.-P. Powder Metallurgical Processing and Characterization of Molybdenum Addition to Tungsten Heavy Alloys by Spark Plasma Sintering. *Materials* **2021**, *14*, 5756. <https://doi.org/10.3390/ma14195756>

Academic Editor: Alain Largeteau

Received: 25 August 2021

Accepted: 27 September 2021

Published: 2 October 2021

Publisher's Note: MDPI stays neutral with regard to jurisdictional claims in published maps and institutional affiliations.



Copyright: © 2021 by the authors. Licensee MDPI, Basel, Switzerland. This article is an open access article distributed under the terms and conditions of the Creative Commons Attribution (CC BY) license (<https://creativecommons.org/licenses/by/4.0/>).

Abstract: The effect of adding molybdenum to the heavy tungsten alloy of W-Ni-Fe on its material characteristics was examined in the current study. The elemental powders of tungsten, iron, nickel, and molybdenum, with a composition analogous to W-3Fe-7Ni-xMo ($x = 0, 22.5, 45, 67.5$ wt.%), were fabricated using the spark plasma sintering (SPS) technique at a sintering temperature of 1400 °C and under pressure of 50 MPa. The sintered samples were subjected to microstructural characterization and tested for mechanical strength. The smallest grain size of 9.99 microns was observed for the 45W-45Mo alloy. This alloy also gave the highest tensile and yield strengths of 1140 MPa and 763 MPa, respectively. The hardness increased with the increased addition of molybdenum. The high level of hardness was observed for 67.5Mo with a 10.8% increase in the base alloy's hardness. The investigation resulted in the alloy of 45W-7Ni-3Fe-45Mo, observed to provide optimum mechanical properties among all the analyzed samples.

Keywords: tungsten heavy alloys; powder metallurgy; spark plasma sintering; materials characteristics

1. Introduction

Traditional tungsten heavy alloys are two-phase composites with W-rich grains and Ni-Fe or Ni-Cu binder phases. The alloy of W-Ni-Fe exhibits good mechanical properties with a rare combination of strength and ductility [1,2]. The fabrication of these alloys is generally achieved through the powder metallurgy technique, with the W phase being dispersed into the Ni-Fe binder to form a matrix phase. While WHAs (tungsten heavy alloys) possess a relatively high density (>17 g/cc), good strength, high-temperature resistance, and thermal stability are also required. They are superior alternatives to other alloys for traditional defense, space, and nuclear applications [3]. In military applications, they are effectively used as kinetic energy penetrators in replacing depleted uranium [4]. They are also used as counterweights and radiation shields.

Alloying additions, such as rhenium, tantalum, cobalt, molybdenum, and oxide-dispersed tungsten heavy alloys, have been explored in some studies [5–8]. The liquid-phase sintered WHA with Re and Mo alloying displayed a suitable refinement of tungsten grains by controlling the grain growth and providing adequate strength and hardness. Cobalt alloying improves the strength of the W-matrix interface and provides solid-solution strengthening. The strength of oxide-dispersed heavy alloys depends on the microstructural development [9]. Yttrium oxide, lanthanum oxide, and thorium oxide with WHAs

show some improvement in alloy hardness [10]. The criterion for molybdenum addition in tungsten heavy alloys controls the grain size by reducing tungsten dissolution in the matrix phase [11]. In a traditional tungsten heavy alloy, the tungsten forms a solid solution with nickel and iron, leading to particle rearrangement in the sintering process. Nickel is a sound activation agent for tungsten. It improves the sintering kinetics by activating the grain boundary diffusion of tungsten [12–14]. Molybdenum forms a eutectic liquid with nickel in the liquid form of W with Ni prematurely, thereby restricting the tungsten's dissolution in the binder phase [15,16]. It provides grain growth inhibition and solid-solution strengthening of the binder phase. The alloying and processing strategies need to be optimized to attain a suitable performance alloy. Heavy tungsten alloys are usually liquid-phase sintered, in which the low melting elements are melted and dispersed over the matrix phase. The W-Ni-Fe alloys are sintered in the temperature range of 1450 °C to 1500 °C with a dwell period of 2 to 5 h, depending on the sintering technique [17]. A longer sintering time leads to a coarse grain microstructure and deterioration of the alloy's mechanical properties. Moreover, fabrication requires post-processing techniques, such as aging and swaging, to improve the heavy alloy's mechanical properties [18–20]. At low-temperature solid-phase sintering, obtaining optimal mechanical properties is necessary to obtain a better performance alloy in as-sintered conditions, thus avoiding post-processing techniques. The spark plasma sintering (SPS) technique processes the heavy tungsten alloys [21]. Due to the rapid heating rate in the process, the powder elements are stimulated, and the sintering process is completed in a significantly shorter time than other sintering techniques. Using the SPS technique, the densification of pure tungsten can be achieved at a lower temperature (1200–1450 °C) [22]. The present work focuses on the W-Ni-Fe alloy's performance with Mo additions using SPS processing at 1400 °C. Molybdenum also possesses a very high melting temperature, good electrical conductivity, outstanding thermal conductivity, corrosion resistance, and a low coefficient of thermal expansion and high hardness [23]. The Mo addition reduces the tungsten composition in the matrix and refines the grain size. The dissolution capacity of Mo in Ni and Fe is higher than that of tungsten [24]. The Ni/Fe ratio in the alloy also affects the material properties by producing different microstructures [25]. If the Ni/Fe ratio is greater than 7:3, the ductility of the material increases, and if it is less, the mechanical characteristics decrease; therefore, a ratio of 7:3 is used to give a stronger yield strength, as investigated by Bose and German. Hence, in this research, the Ni/Fe ratio is maintained at 7:3, and Mo is varied at different ratios with tungsten. Without tungsten, one alloy (90Mo-7Ni-3Fe) was produced and analyzed to determine the difference between tungsten-added alloys and tungsten-less alloys and whether molybdenum may replace tungsten without sacrificing mechanical characteristics.

2. Methods and Materials

Tungsten, molybdenum, nickel, and iron, as the received powders, have an average particle size of 12 µm, <150 µm, <150 µm, and 9 µm, respectively. All of the powders were purchased from Sigma Aldrich, India. Figure 1 shows the SEM morphology of tungsten's metal powders, molybdenum, nickel, and iron. The powder characteristics are listed in Table 1. The Ni-Fe ratio is maintained at 7:3, and Mo content is varied as 0%, 22.5%, 45%, 67.5% and 90% (composition shown in Table 2). V-Mixer and Ball Mill (without the ball) were used to blend the powders. The given compositions' consolidation was performed with using the SPS machine (model: DR. Sinter) (Fuji Electronic Industrial Co. Ltd., Tsurugashima Saitama, Japan). Graphite dies with a 30 mm internal diameter were used for the compaction process. A thin foil of graphite was used to distinguish the powder and the punch from the die for the effortless removal of sintered compact. Before sintering, a vacuum was generated in the furnace, which was then filled with argon gas, and the process was repeated three times to achieve a final vacuum of 2 Pa. The powder was sintered at 1400 °C under the uniaxial pressure of 50 MPa, using a heating rate of 100 °C/min. The pressure was maintained over the powder compact during the whole period of the SPS process. The sintering temperature of 1400 °C was maintained

in the furnace for five minutes, after which the samples were allowed to cool down in the furnace. The samples with a 30 mm diameter and 7 mm height were produced. The relative sintered density of the samples was determined using the Archimedes principle. Sintered alloys were polished using SiC emery sheets of different grit sizes ranging from 220 to 1200. Diamond paste (6 μm particles) was later used to achieve the sample's surface mirror finish. Murakami's reagent (100 mL distilled water, 10 g $\text{K}_3\text{Fe}(\text{C.N.})_6$, and 10 g KOH) was applied over the polished samples for etching to highlight the grain boundaries. An optical microscope (Zeiss, Oberkochen, Germany) was used to capture micrographs of sintered samples. A scanning electron microscope (SEM, ZEISS EVO 180, Oberkochen, Germany) was used to obtain micro-images with greater magnification.

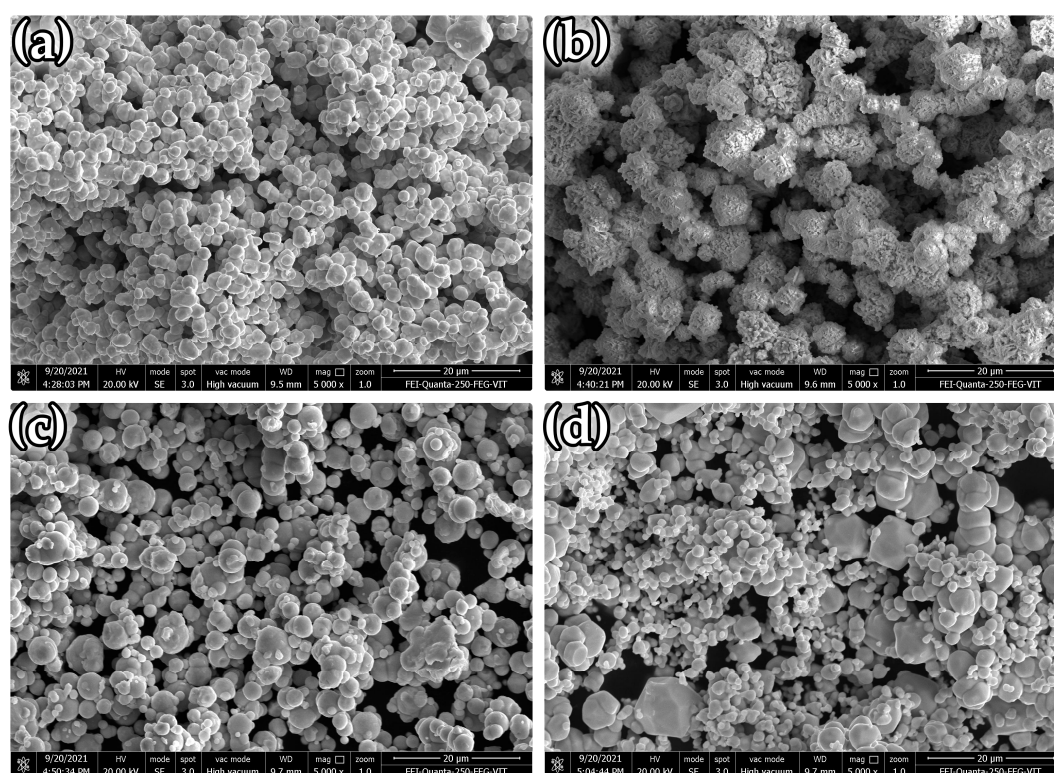


Figure 1. Powder morphology of (a) tungsten, (b) nickel, (c) iron, and (d) molybdenum.

Table 1. Characteristics of W, Mo, Ni, and Fe metal powders.

Powder	W	Mo	Ni	Fe
Particle Size (μm)	12 ± 4	150 ± 5	150 ± 5	9 ± 6
Particle Shape	Irregular	Irregular	Spherical	Spherical
Purity %	99.9	99.9	99.9	99.9
Density (g/cm^3)	19.28	10.3	8.91	7.86

Table 2. Compositions of samples and experimental parameters.

Set No.	Composition	W/Mo Ratio	Compaction Pressure	Heating Rate
1	90W-7Ni-3Fe	100:1	50 MPa	100 $^{\circ}\text{C}/\text{min}$
2	67.5W-22.5Mo-7Ni-3Fe	75:25	50 MPa	100 $^{\circ}\text{C}/\text{min}$
3	45W-45Mo-7Ni-3Fe	50:50	50 MPa	100 $^{\circ}\text{C}/\text{min}$
4	22.5W-67.5Mo-7Ni-3Fe	25:75	50 MPa	100 $^{\circ}\text{C}/\text{min}$
5	90Mo-7Ni-3Fe	1:100	50 MPa	100 $^{\circ}\text{C}/\text{min}$

Energy dispersive X-ray spectrometer (EDS) graphs were obtained simultaneously. The elemental composition of the individual metals was studied using the elemental mapping method. Measurement of the micro-hardness of the sintered samples was conducted with a micro-Vickers hardness tester (Leco, micro-Vickers hardness tester LM248AT, St. Joseph, MI, USA) with an indentation load (0.5 kgf) for a dwell period of ten seconds. Ten readings were taken for each sample by creating indents on the surface at ten random locations. The test result was achieved by calculating the mean of the ten readings. The average grain size was measured using the SEM micrographs taken from the samples [26]. The contiguity (C_{WW}) was calculated by measuring the number of W–W grain connections (N_{WW}) and W–Ni–Fe–Mo interfaces (N_{WM}) using the line-intercept method [27] as given below:

$$C_{WW} = \frac{2N_{WW}}{2N_{WW} + N_{WM}} \quad (1)$$

The mechanical properties of UTS (Ultimate Tensile Strength), % elongation, and yield strength were measured using a tensile testing machine (INSTRON 8801, Norwood, MA, USA) following MPIF specifications. The rate of strain used was $3.29 \times 10^{-4} \text{ s}^{-1}$ (cross-head speed 0.5 mm/min).

3. Results and Discussion

3.1. Densification Behavior of the Sintered Samples

The densification behavior showed an increase in the alloy's relative density with an increase in Mo content, as shown in Figure 2. The process comprised particle rearrangement, dissolution, and precipitation over the binding and diffusion mechanisms at the boundary dividing the matrix phase [28,29]. A maximum relative density of 89.26% was obtained for the 90 wt.% addition of molybdenum. A 15% increase was observed compared to the base alloy. The spark plasma sintering process also aided in improving the sintering kinetics by activating the particles at a high heating rate. The density obtained is in accordance with observations made in other studies on heavy tungsten alloys with molybdenum [30,31].

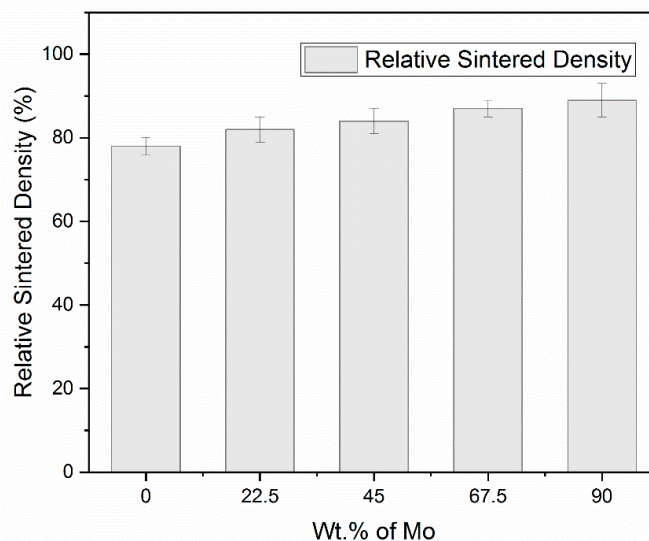


Figure 2. Graphical representation of variation in sintered density with the increase in molybdenum concentration.

3.2. Microstructure Analysis

Molybdenum's addition to WHAs of W–Ni–Fe resulted in changes in the tungsten dissolution in the matrix phase. The contents of the sample were verified in the EDS spectrum, as represented in Figure 3. The microstructure of the sintered samples obtained by varying the proportion of molybdenum is shown in Figure 4. The SEM BSE (backscattered electron) microstructures showed four distinct regions: white tungsten rich phase, light

grey molybdenum rich phase, dark grey Ni-Fe rich phase, and pores represented as a thick darker region [32]. The alloy of 90W-7Ni-3Fe showed lesser and non-uniform diffusion of tungsten in the matrix phase with sharp undissolved boundaries visible in the structure. With the addition of molybdenum, more spheroidization and refinement of tungsten grain size were observed.

Mo-added microstructures with a small grain size are shown in Figure 4. The dissolution of tungsten and molybdenum in the Ni-Fe matrix phase evolved with the sintering temperature and time. Molybdenum has very low solubility with tungsten, but it has a greater nickel than W in Ni. At 1100 °C, the Mo solubility in Ni is 25 at.% and that of W in Ni is 16.4 at.% [33]. Thus, the tungsten concentration in the matrix phase was reduced, the microstructure was refined, and the Mo addition improved the solid-solution strengthening of the binder phase.

In all of the alloys, micropores were observed. Porosity is the biggest issue in powder metallurgy-processed components. In all of the alloys, pores are equally distributed throughout the material due to equal heat distribution, but the fraction of porosity is different. The shape of the pores is irregular. Pores act as stress raisers, and they deteriorate the properties of materials.

The samples' elemental mapping is shown in Figure 5a,b to verify the distribution of different elemental contents. The variations in grain size, binder volume fraction, and contiguity are all tabulated in Table 3. The grain size of molybdenum-added alloys was observed to be lesser than the base alloy's size without Mo addition. The smallest grain size of 9.99 microns was obtained for the W-45Mo-7Ni-3Fe alloy. A higher value of 10.22 microns was observed for the 67.5 wt.% Mo-added alloy. This increase is attributed to the change in the matrix volume fraction and the variation in tungsten dissolution in the matrix phase [34]. The spark plasma sintering process also contributed to grain size control. The high heating rate reduced the diffusion process's total time in the conventional sintering technique and minimized the grain coarsening effect. The contiguity of the W-Ni-Fe alloy was measured to be 0.6093. For molybdenum-added heavy alloys, the contiguity varied from 0.43 to 0.59, which is smaller than the base alloy's value. Generally, microstructures with minimal contiguity are perceived to provide alloys with good strength and ductility [35]. A high contiguity value represents higher W-W contacts, leading to the phases' brittleness and thereby reducing the alloy's ductility. The obtained contiguity values are in accordance with those in the literature on heavy tungsten alloys ranging from 0.4 to 0.6 [36,37]. The matrix volume fraction for the molybdenum-added alloys showed a variation between 32% and 47%. The volume fraction increased with an increase in Mo addition up to 45 wt.%, and there was a corresponding decrease in the microstructure's contiguity [37].

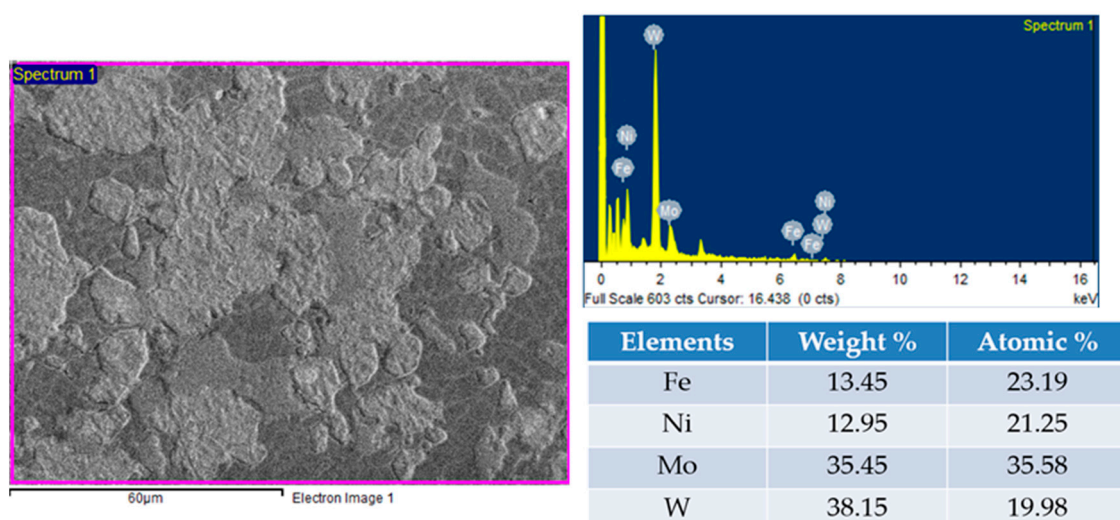


Figure 3. Energy dispersive X-ray spectroscopy of the 45W-7Ni-3Fe-45Mo alloy.

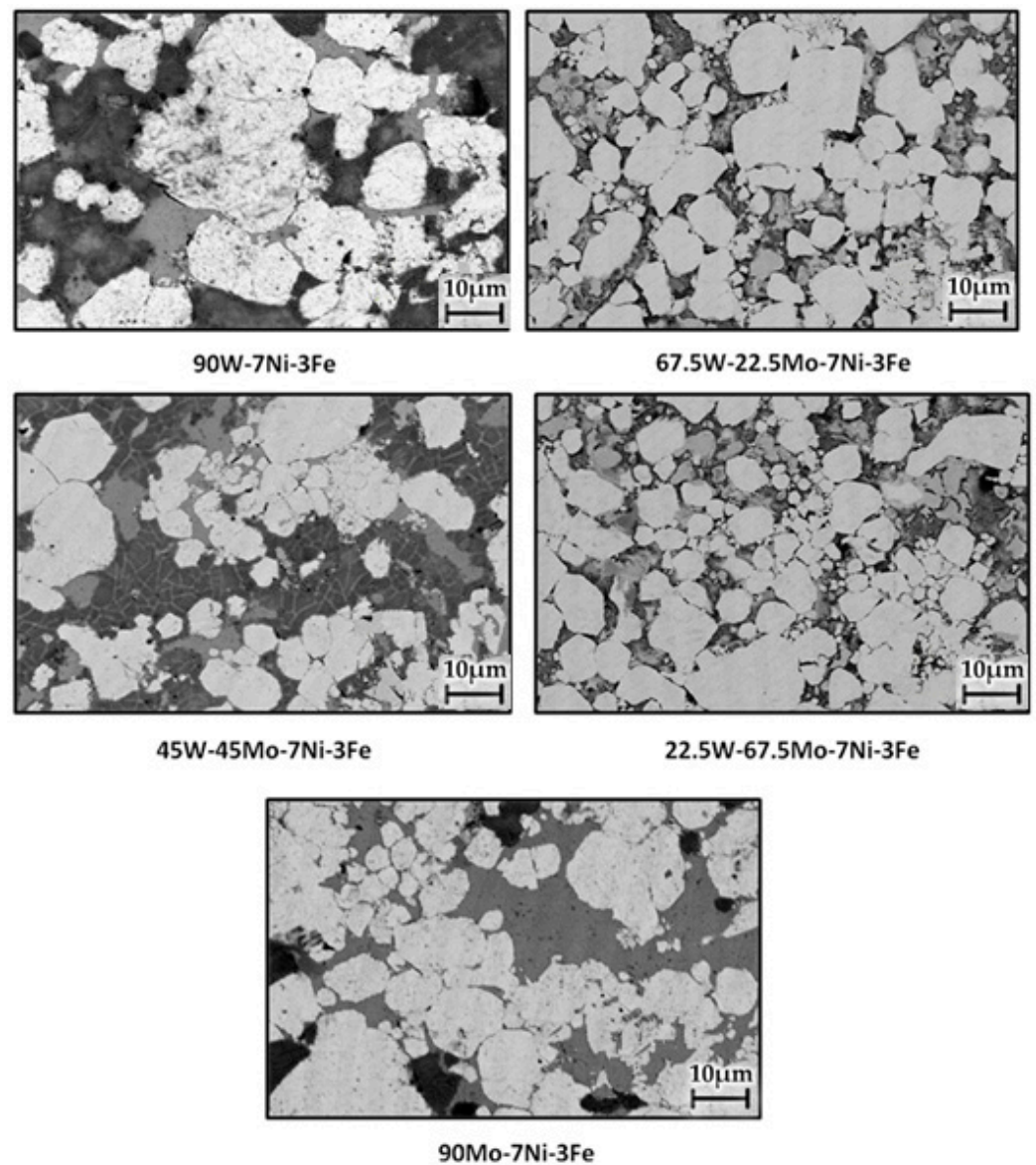


Figure 4. SEM (BSE mode) micrographs of alloys with the increase in molybdenum concentration.

Table 3. Relative sintered density, grain size, and contiguity of all sintered heavy alloys.

S. No.	Specimen Composition (%)	Relative Sintered Density (%)	Grain Size (μm)	Contiguity
1	90W-7Ni-3Fe	78 ± 2	11 ± 5	0.60 ± 0.06
2	67.5W-22.5Mo-7Ni-3Fe	82 ± 3	10. ± 2	0.59 ± 0.08
3	45W-45Mo-7Ni-3Fe	84 ± 3	10 ± 3	0.47 ± 0.1
4	22.5W-67.5Mo-7Ni-3Fe	87 ± 2	10 ± 4	0.43 ± 0.09
5	90Mo-7Ni-3Fe	89 ± 4	10 ± 2	0.57 ± 0.06

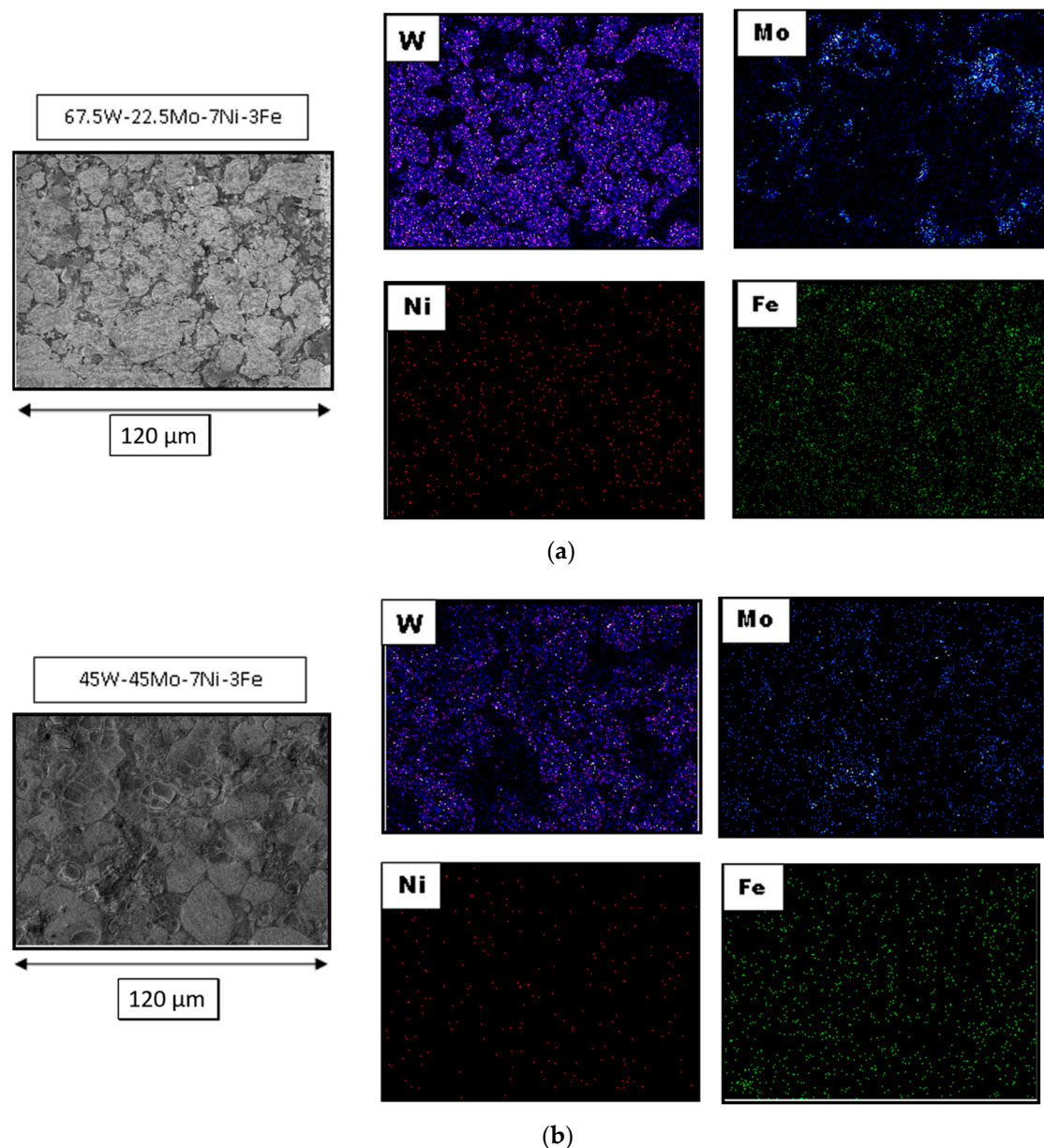


Figure 5. (a) Elemental mapping of 67.5W-22.5Mo-7Ni-3Fe, (b) elemental mapping of 45W-45Mo-7Ni-3Fe.

3.3. Mechanical Properties

Heavy tungsten alloys can provide good mechanical properties with a Ni/Fe ratio of 7:3 [25]. The experimental results of tensile strength, yield strength, hardness, and % elongation of the alloys are presented in Table 4. The molybdenum's ultimate tensile strength added to the tungsten heavy alloys was higher than the alloy without Mo addition. The alloy W-45Mo-7Ni-3Fe exhibited the highest tensile strength of 1140 MPa and a corresponding yield strength of 763 MPa. The sintering and microstructural parameters influence the strength of alloys [38,39]. Rapid heating is followed in the SPS process, resulting in a reduced coarsening of the grains [30]. The refined grain size also contributes to the alloy's good yield strength based on the Hall–Petch concept [40]. With a reduced grain size, the possible movement of the dislocations created at the grain boundaries restricted the plastic deformation [41]. The lower yield strengths of W-Ni-Fe and Mo-Ni-Fe can be attributed to the corresponding larger grain size and contiguity factors.

Table 4. Mechanical properties of all sintered alloys.

Sr. No	Specimen Label	UTS (MPa)	Yield Strength (MPa)	Elongation (%)	Micro-Vickers Hardness (Hv _{0.5})
1	90W-7Ni-3Fe	702 ± 13	442 ± 26	0.17 ± 0.05	544 ± 24
2	67.5W-22.5Mo-7Ni-3Fe	1077 ± 33	722 ± 40	1.51 ± 0.06	595 ± 31
3	45W-45Mo-7Ni-3Fe	1140 ± 26	763 ± 38	0.89 ± 0.08	613 ± 26
4	22.5W-67.5Mo-7Ni-3Fe	815 ± 20	546 ± 40	0.55 ± 0.08	653 ± 19
5	90Mo-7Ni-3Fe	528 ± 54	492 ± 29	0.54 ± 0.04	560 ± 22

The hardness of sintered alloys reflects a growing pattern in the improvement in molybdenum content in alloys. The heavy alloy of W-67.5Mo-7Ni-3Fe contributed to the maximum hardness of 653 Hv, with a significant increase of 10.8% in the hardness (544 Hv) of the heavy tungsten alloy without molybdenum. The Mo addition generally provided a substantial solution strengthening of the binder and improved the cohesion between the tungsten grains and the Ni-Fe-Mo matrix. The ductility of the alloys did not indicate a significant difference with the inclusion of molybdenum. However, the ductility of W-Mo-Ni-Fe alloys was higher than that of the W-Ni-Fe alloy, and a decreasing trend was observed with an increase in molybdenum percentage. This trend is similar to the observations made in other studies on tungsten heavy alloys with Mo addition [30,31]. Mo was highly soluble in the matrix compared to W. As Mo content increased, the solubility of Mo in the matrix increased, and the solubility of W in the matrix decreased, which deteriorated the mechanical properties. When the content of Mo in the alloy was above 45 wt.%, the tensile strength decreased [42].

4. Conclusions

The effect of molybdenum alloying with the W-Ni-Fe tungsten heavy alloy was investigated in this research. The results revealed that the yield and tensile strength of W-Ni-Fe-Mo alloys showed a significant improvement compared to those of the W-Ni-Fe alloy. The molybdenum addition provided grain growth inhibition and solid-solution strengthening of the matrix phase, and restricted tungsten phase dissolution. Mo has a higher solubility than that of W. The grain size of the W-Ni-Fe-Mo alloy decreased with an increase in molybdenum content. The alloy W-45Mo-7Ni-3Fe exhibited the highest tensile strength of 1140 MPa and corresponding yield strength of 763 MPa. It was also observed that with the increase in molybdenum in the alloy, the degree of tungsten spheroidization increased. The increase in Mo content also influenced the hardness property, showing a corresponding increasing trend. The maximum hardness was observed for W-67.5Mo-7Ni-3Fe with a 10.8% increase from the base alloy's hardness. The ultimate tensile strength of the 45% W and 45% Mo alloy was 62% more than that of the parent alloy.

Author Contributions: Conceptualization, A.M. and A.R.A.; methodology, A.R.A., A.M. and S.A.; formal analysis, M.S.; investigation, A.R.A. and A.M.; resources, A.R.A. and C.-P.J.; data curation, S.A. and A.K.; writing—original draft preparation, A.R.A., S.N., S.A. and A.K.; writing—review and editing, A.M., A.R.A. and M.S.; supervision, A.M. and A.R.A.; project administration, A.R.A. and C.-P.J.; funding acquisition, C.-P.J. All authors have read and agreed to the published version of the manuscript.

Funding: This research was funded by Ministry of Science and Technology of China (Taiwan), under grant numbers MOST 109-2221-E-194-011-MY2 and MOST 109-2923-E-194-002-MY3.

Institutional Review Board Statement: Not applicable.

Informed Consent Statement: Not applicable.

Data Availability Statement: Not applicable.

Conflicts of Interest: The authors declare no conflict of interest.

References

- Khalid, F.A.; Bhatti, M.R. Microstructure and Properties of Sintered Tungsten Heavy Alloys. *J. Mater. Eng. Perform.* **1999**, *8*, 46–50. [\[CrossRef\]](#)
- Sahin, Y. Recent Progress in Processing of Tungsten Heavy Alloys. *J. Powder Technol.* **2014**, *2014*, 764306.
- Bose, A.; German, R.M. Matrix composition effects on the tensile properties of tungsten-molybdenum heavy alloys. *Metall. Mater. Trans. A* **1990**, *21*, 1325–1327. [\[CrossRef\]](#)
- Upadhyaya, A.; Tiwari, S.K.; Mishra, P. Microwave sintering of W-Ni-Fe alloy. *Scr. Mater.* **2007**, *56*, 5–8. [\[CrossRef\]](#)
- Kiran, U.R.; Panchal, A.; Kumar, M.P.; Sankaranarayana, M.; Rao, G.N.; Nandy, T.K. Refractory metal alloying: A new method for improving heavy tungsten alloys' mechanical properties. *J. Alloys Compd.* **2017**, *709*, 609–619. [\[CrossRef\]](#)
- Senthilnathan, N.; Annamalai, A.R.; Venkatachalam, G. Microstructure and mechanical properties of spark plasma sintered tungsten heavy alloys. *Mater. Sci. Eng. A* **2018**, *710*, 66–73. [\[CrossRef\]](#)
- Jing-Lian, F.; Tao, L.; Hui-Chao, C.; Deng-Long, W. Preparation of fine grain tungsten heavy alloy with high properties by mechanical alloying and yttrium oxide addition. *J. Mater. Process. Technol.* **2008**, *208*, 463–469. [\[CrossRef\]](#)
- Aguirre, M.; Martín, A.; Pastor, J.; Llorca, J.; Monge, M.; Pareja, R. Mechanical properties of tungsten alloys with Y₂O₃ and titanium additions. *J. Nucl. Mater.* **2011**, *417*, 516–519. [\[CrossRef\]](#)
- Lee, K.H.; Cha, S.I.; Ryu, H.J.; Hong, S.H. Effect of oxide dispersoids and mechanical properties of heavy tungsten alloy fabricated by the mechanical alloying process. *Mater. Sci. Eng. A* **2007**, *452*, 55–60. [\[CrossRef\]](#)
- AyyappaRaj, M.; Yadav, D.; Agrawal, D.K.; Rajan, R.A.A. Microstructure and mechanical properties of spark plasma-sintered La₂O₃ dispersion-strengthened W-Ni-Fe alloy. *Rare Met.* **2020**, *40*, 2230–2236. [\[CrossRef\]](#)
- Kemp, P.; German, R. Grain growth in liquid-phase-sintered W-Mo-Ni-Fe alloys. *J. Less Common Met.* **1991**, *175*, 353–368. [\[CrossRef\]](#)
- Gurwell, W.; Nelson, R.; Dudder, G.; Davis, N. *Fabrication and Properties of Tungsten Heavy Metal Alloys Containing 30% to 90% Tungsten*; Pacific Northwest Lab.: Richland, WA, USA, 1984.
- Ćirović, N.; Spasojević, P.; Ribić-Zelenović, L.; Maričić, A.; Spasojević, M. Synthesis, Structure, and Properties of Nickel-Iron-Tungsten Alloy Electrodeposits PART II: Effect of Microstructure on Hardness, Electrical, and Magnetic Properties. *Sci. Sinter.* **2016**, *48*, 1–16. [\[CrossRef\]](#)
- Chausse, C.; Nardou, F. Evolution of the microstructure in a W alloy during sintering before the formation of a liquid phase. *Mater. High Temp.* **1999**, *16*, 37–41. [\[CrossRef\]](#)
- Massalski, T.B.; Murray, J.L.; Bennett, L.H.; Baker, H. *Binary Alloy Phase Diagrams*; American Society for Metals: Metals Park, OH, USA, 1990; Volume 1, p. 1100.
- Kiran, U.R.; Panchal, A.; Sankaranarayana, M.; Nandy, T.K. Tensile and impact behavior of swaged tungsten heavy alloys processed by liquid phase sintering. *Int. J. Refract. Met. Hard Mater.* **2013**, *37*, 1–11. [\[CrossRef\]](#)
- Senthilnathan, N.; Annamalai, A.R.; Venkatachalam, G. Sintering of Tungsten and Tungsten Heavy Alloys of W-Ni-Fe and W-Ni-Cu: A Review. *Trans. Indian Inst. Met.* **2017**, *70*, 1161–1176. [\[CrossRef\]](#)
- Durlu, N.; Çalişkan, N.K.; Bor, Ş. Effect of swaging on microstructure and tensile properties of W-Ni-Fe alloy. *Int. J. Refract. Met. Hard Mater.* **2014**, *42*, 126–131. [\[CrossRef\]](#)
- Yu, Y.; Zhang, W.; Chen, Y.; Wang, E. Effect of swaging on microstructure and mechanical properties of liquid phase sintered 93W-4.9(Ni, Co)-2.1Fe alloy. *Int. J. Refract. Met. Hard Mater.* **2014**, *44*, 103–108. [\[CrossRef\]](#)
- Kim, D.-K.; Lee, S.; Noh, J.-W. Dynamic and quasi-static torsional behavior of tungsten heavy alloy specimens fabricated through sintering, heat-treatment, swaging and aging. *Mater. Sci. Eng. A* **1998**, *247*, 285–294. [\[CrossRef\]](#)
- Hu, K.; Li, X.; Qu, S.; Li, Y. Spark-plasma sintering of W-5.6Ni-1.4Fe heavy alloys: Densification and grain growth. *Metall. Mater. Trans. A* **2013**, *44*, 923. [\[CrossRef\]](#)
- Deng, S.; Yuan, T.; Li, R.; Zeng, F.; Liu, G.; Zhou, X. Spark plasma sintering of pure tungsten powder: Densification kinetics and grain growth. *Powder Technol.* **2017**, *310*, 264–271. [\[CrossRef\]](#)
- Xiao, M.; Li, F.; Xie, H.; Wang, Y. Characterization of strengthening mechanism and hot deformation behavior of powder metallurgy molybdenum. *Mater. Des.* **2012**, *34*, 112–119. [\[CrossRef\]](#)
- Hsu, C.S.; Lin, K.H.; Lin, S.T. Precipitation mechanisms of intermetallic compounds. *Int. J. Refract. Met. Hard Mater.* **2005**, *23*, 175–182. [\[CrossRef\]](#)
- German, R.M. *Microstructure and Impurity Effects on Tungsten Heavy Alloys*; Final Report, AD-A224 220, Contract Number DAAL01-87-K-0072; U.S. Army Research Office, Aberdeen Proving Ground: Harford County, MD, USA, 1990.
- Standard Test Methods for Determining Average Grain Size*; ASTM E112-96; ASTM: Philadelphia, PA, USA, 1996; Volume 16.
- Gurland, J. The measurement of grain contiguity in two-phase alloys. *Trans. Met. Soc. AIME* **1958**, *212*, 452–455.
- Gong, X.; Fan, J.; Ding, F.; Song, M.; Huang, B. Effect of tungsten content on microstructure and quasi-static tensile fracture characteristics of rapidly hot-extruded W-Ni-Fe alloys. *Int. J. Refract. Met. Hard Mater.* **2012**, *30*, 71–77. [\[CrossRef\]](#)
- Lee, G.; McKittrick, J.; Ivanov, E.; Olevsky, E. Densification mechanism and mechanical properties of tungsten powder consolidated by spark plasma sintering. *Int. J. Refract. Met. Hard Mater.* **2016**, *61*, 22–29. [\[CrossRef\]](#)
- Prasad, B.S.L.; Annamalai, R. A study of molybdenum addition on W-Ni-Fe based heavy alloys sintered with spark plasma sintering. *Bull. Pol. Acad. Sci. Tech. Sci.* **2019**, *67*, 167–172.

31. Muthuchamy, A.; Yadev, D.; Agrawal, D.K.; Annamalai, R. Structure-property correlations of W-Ni-Fe-Mo heavy alloys consolidated using spark plasma sintering. *Mater. Res. Express* **2018**, *6*, 026545. [[CrossRef](#)]
32. Hsu, C.-S.; Lin, S.-T. Effect of molybdenum on grain growth of W-Mo-Ni-Fe heavy alloys. *J. Mater. Sci.* **2003**, *38*, 1543–1549. [[CrossRef](#)]
33. Bose, A.; German, R.M. *Properties of Aged and Swaged Molybdenum Doped Heavy Alloys*; Materials Engineering Department Rensselaer Polytechnic Institute: Troy, NY, USA, 1998; Volume 19, pp. 139–153.
34. Senthilnathan, N.; Raja Annamalai, A.R.; Venkatachalam, G. Effect of cobalt addition on the morphology and mechanical properties of W-Ni-Cu-Co alloy. *Emerg. Mater. Res.* **2019**, *8*, 558–566. [[CrossRef](#)]
35. Li, X.; Hu, K.; Qu, S.; Li, L.; Yang, C. 93W–5.6Ni–1.4Fe heavy alloys with enhanced performance prepared by cyclic spark plasma sintering. *Mater. Sci. Eng. A* **2014**, *599*, 233–241. [[CrossRef](#)]
36. Ding, L.; Xiang, D.; Li, Y.; Li, C.; Li, J. Effects of sintering temperature on fine-grained tungsten heavy alloy produced by high-energy ball milling assisted spark plasma sintering. *Int. J. Refract. Met. Hard Mater.* **2012**, *33*, 65–69. [[CrossRef](#)]
37. Kumari, A.; Sankaranarayana, M.; Nandy, T.K. On structure-property correlation in high strength tungsten heavy alloys. *Int. J. Refract. Met. Hard Mater.* **2017**, *67*, 18–31. [[CrossRef](#)]
38. Li, Y.; Hu, K.; Li, X.; Ai, X.; Qu, S. Fine-grained 93W–5.6Ni–1.4Fe heavy alloys with enhanced performance prepared by spark plasma sintering. *Mater. Sci. Eng. A* **2013**, *573*, 245–252. [[CrossRef](#)]
39. Laptev, A.V. Structure and properties of WC-Co alloys in solid-phase sintering. *Powder Metall. Met. Ceram.* **2007**, *46*, 517–524. [[CrossRef](#)]
40. Kim, J.Y.; Jang, D.; Greer, J.R. Tensile and compressive behavior of tungsten, molybdenum, tantalum, and niobium the nanoscale. *Acta Mater.* **2010**, *58*, 2355–2363. [[CrossRef](#)]
41. Hansen, N. Hall-Petch relation and boundary strengthening. *Scr. Mater.* **2004**, *51*, 801–806. [[CrossRef](#)]
42. Lin, K.-H.; Hsu, C.-S.; Lin, S.-T. Precipitation of an Intermetallic Phase in Mo-alloyed Tungsten Heavy Alloys. *Mater. Trans.* **2003**, *44*, 358–366. [[CrossRef](#)]

Article

High Pressure (HP) in Spark Plasma Sintering (SPS) Processes: Application to the Polycrystalline Diamond

Jérémy Guignard *, Mythili Prakasam * and Alain Largeteau * 

CNRS, Bordeaux INP, ICMCB, UMR 5026, University of Bordeaux, F-33600 Pessac, France

* Correspondence: jeremy.guignard@icmcb.cnrs.fr (J.G.); mythili.prakasam@icmcb.cnrs.fr (M.P.); alain.largeteau@u-bordeaux.fr (A.L.)

Abstract: High-Pressure (HP) technology allows new possibilities of processing by Spark Plasma Sintering (SPS). This process is mainly involved in the sintering process and for bonding, growing and reaction. High-Pressure tools combined with SPS is applied for processing polycrystalline diamond without binder (binderless PCD) in this current work. Our described innovative Ultra High Pressure Spark Plasma Sintering (UHP-SPS) equipment shows the combination of our high-pressure apparatus (Belt-type) with conventional pulse electric current generator (Fuji). Our UHP-SPS equipment allows the processing up to 6 GPa, higher pressure than HP-SPS equipment, based on a conventional SPS equipment in which a non-graphite mold (metals, ceramics, composite and hybrid) with better mechanical properties (capable of 1 GPa) than graphite. The equipment of UHP-SPS and HP-SPS elements (pistons + die) conductivity of the non-graphite mold define a Hot-Pressing process. This study presents the results showing the ability of sintering diamond powder without additives at 4–5 GPa and 1300–1400 °C for duration between 5 and 30 min. Our described UHP-SPS innovative cell design allows the consolidation of diamond particles validated by the formation of grain boundaries on two different grain size powders, i.e., 0.75–1.25 µm and 8–12 µm. The phenomena explanation is proposed by comparison with the High Pressure High Temperature (HP-HT) (Belt, toroidal-Bridgman, multi-anvils (cubic)) process conventionally used for processing binderless polycrystalline diamond (binderless PCD). It is shown that using UHP-SPS, binderless diamond can be sintered at very unexpected P-T conditions, typically ~10 GPa and 500–1000 °C lower in typical HP-HT setups. This makes UHP-SPS a promising tool for the sintering of other high-pressure materials at non-equilibrium conditions and a potential industrial transfer with low environmental fingerprints could be considered.



Citation: Guignard, J.; Prakasam, M.; Largeteau, A. High Pressure (HP) in Spark Plasma Sintering (SPS) Processes: Application to the Polycrystalline Diamond. *Materials* **2022**, *15*, 4804. <https://doi.org/10.3390/ma15144804>

Academic Editor: Miguel Alguero

Received: 27 June 2022

Accepted: 7 July 2022

Published: 9 July 2022

Publisher's Note: MDPI stays neutral with regard to jurisdictional claims in published maps and institutional affiliations.



Copyright: © 2022 by the authors. Licensee MDPI, Basel, Switzerland. This article is an open access article distributed under the terms and conditions of the Creative Commons Attribution (CC BY) license (<https://creativecommons.org/licenses/by/4.0/>).

Keywords: high pressure; Spark Plasma Sintering; binderless diamonds

1. Introduction

Spark Plasma Sintering (SPS) is a well-known sintering technique born in Japan in the 60s that consists of using pulsed current injected into a powder to be sintered [1,2]. Since then, a lot of development through different patents [3] has been made and a different generation of SPS succeeded to the current fifth generation of SPS that allows industrialization of the process [3,4].

Conventional SPS (conv-SPS) is widely used in materials sciences [4] and is starting to be used by experimental petrologists [5]. Typically, suitable materials for SPS are metals, ceramics, composites and even organic materials. Basically, the principle of SPS is similar to that of hot pressing (HPing), the main difference being the heating procedure of the starting materials. Powder is loaded into a graphite die and enclosed by two graphite punches (Figure 1). Rarely, powder is packed in WC/Co die and pistons for higher pressure but lower temperature purposes (Figure 1). The assembly is then placed between two electrodes that are used to apply pressure (typically up to 100 MPa) and to inject the current through the graphite (WC/Co) mold and the powder. It is of note that graphite or WC/Co

ensures hydrostaticity and acts as furnace. Heating occurs therefore by the Joule effect and the injected current inside the powder has a significant effect that depends on the materials. Typically, for non-conductive materials, the electric charge accumulates at the surface particles, favoring surface diffusion, particles breakdown and formation of grain boundaries [6–8]. As a consequence, densification occurs at a lower temperature.

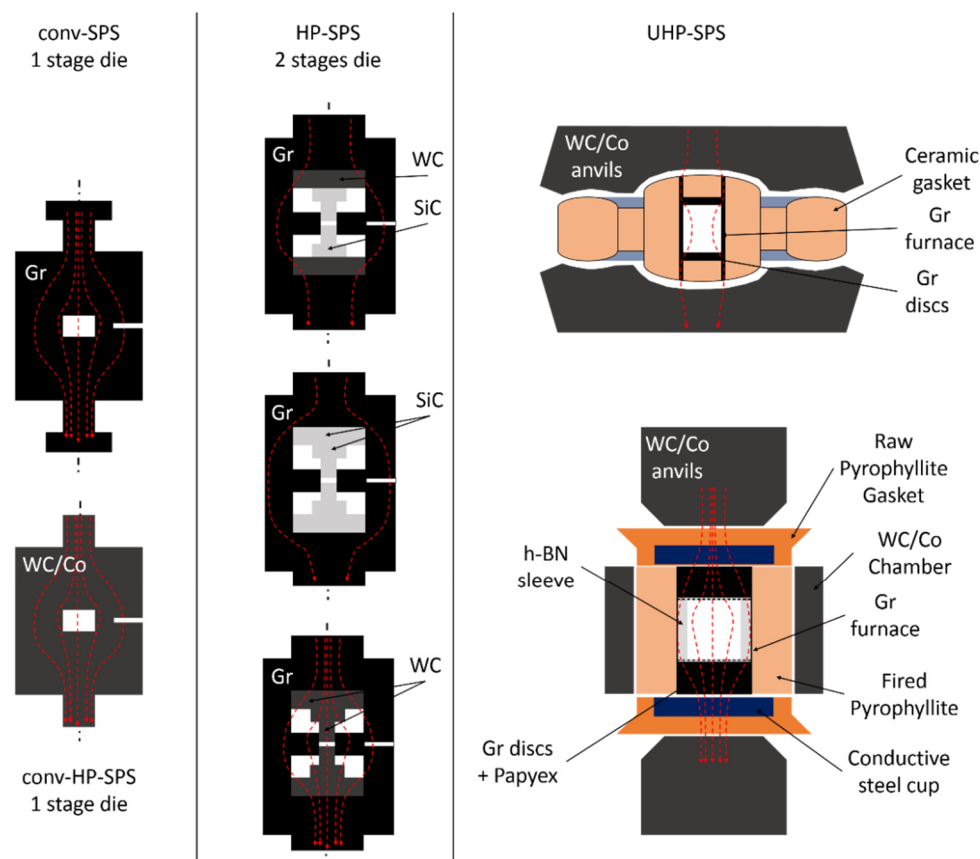


Figure 1. Drawing representing the different SPS assemblies and pathways of the injected current (red arrows). Conv-SPS assemblies (**left columns**) showing the mold contents, the sample and the furnace. These assemblies consist of mold mostly in graphite (Gr) to reach $P_{max} = 0.1 \text{ GPa}$ and $T_{max} \sim 2500 \text{ }^{\circ}\text{C}$ and for HP-SPS in WC/Co to reach $P_{max} = 1 \text{ GPa}$ at low temperature ($100\text{--}200 \text{ }^{\circ}\text{C}$) (higher temperature for lower pressure is also possible). HP-SPS special assemblies (**middle columns**) in conventional equipment are more sophisticated and consist of double stage mold with an outer shell (acting as furnace) and inner die in graphite with hard materials discs/pistons (SiC and or binderless WC). In that case, $P_{max} = 1 \text{ GPa}$ and $T_{max} = 1100 \text{ }^{\circ}\text{C}$ can be reached but the current pathway depends on the composition of pistons and discs. Therefore, the SPS process does not necessarily occur. In UHP-SPS setups (**right column**), assemblies are much more complicated to ensure good hydrostaticity. Typically, a ceramic cell is used to receive a thin wall graphite furnace in which powder is loaded. Powder is then packed between graphite punches inside the graphite tube furnace that allow current injection inside the sample (SPS principle). Hence, $P_{max} = 6\text{--}8 \text{ GPa}$ and $T_{max} = 2000 \text{ }^{\circ}\text{C}$ can be achieved.

Pressure (P) is, like temperature (T), a fundamental driving force that can favor a lot of different physical and chemical processes that can optimize properties of materials such as mechanical, optical and thermal.

Indeed, a lot of different physical and chemical processes obey to a temperature and/or pressure activation that can be described for example as an Arrhenius-type equation (Figure 2):

$$A = A_0 \times e^{\left(-\frac{Q+PV}{RT}\right)} \quad (1)$$

where A is the process, that can be for example, a diffusion coefficient, a grain growth rate, a grain boundary formation rate, a reaction kinetic, etc. In this Equation (1), A_0 is pre-exponential term, P is the pressure (in Pa), T is the temperature (in K) and R the perfect gas constant ($R = 8.314 \text{ J mol}^{-1} \text{ K}^{-1}$). The most interesting terms here are the activation energy (Q in J mol^{-1}) and activation volume (V in $\text{m}^3 \text{ mol}^{-1}$). Thus, high pressure can start the activation of a given process A at several hundred degrees lower than at ambient pressure (Figure 2).

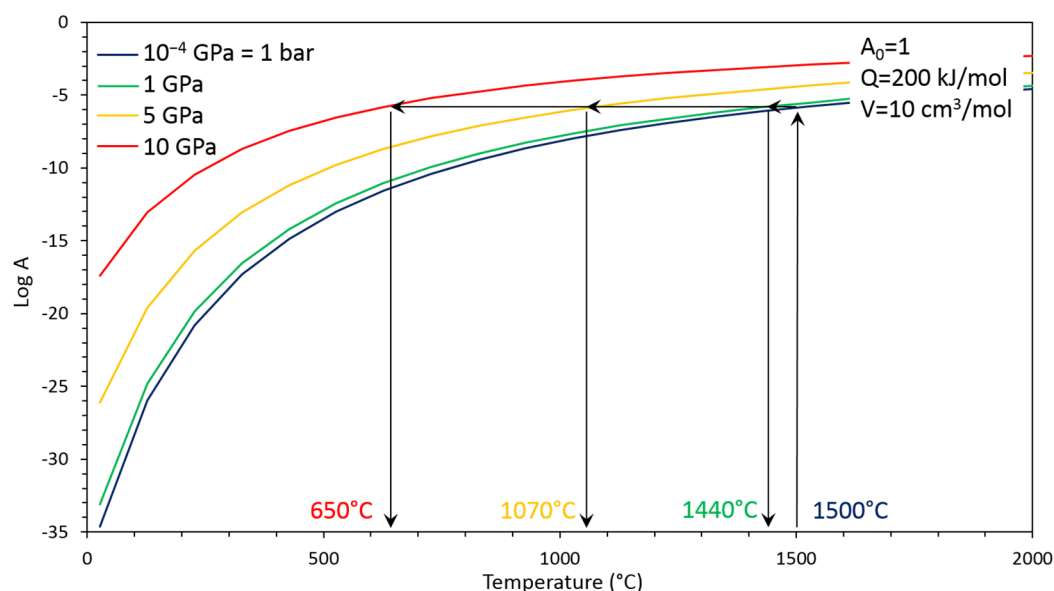


Figure 2. Graphic illustration of Equation (1) showing the efficiency of pressure (colored curves) to activate a physical or chemical process A as a function of temperature. Starting parameters A_0 , Q and V have been chosen arbitrary for illustration purposes. Sintering can be activated at several hundred degrees lower when applying high pressure of few GPa than at 1 bar (10^{-4} GPa).

In particularly, pressure allows the synthesis of materials, even with different thermal stabilities precursors [9]:

- to orientate the chemical reaction in the direction of synthesis leading to the densest phase by the Le Chatelier principle (ex: synthesis of diamond to the detriment of graphite), e.g., [10,11];
- to initiate a new finer microstructure by driving the phase transformation in polymorphic materials (ex: Al_2O_3 : $\gamma \rightarrow \alpha$), e.g., [12,13];
- to improve the chemical reactivity for refractory materials sintering (borides, nitrides, carbides) to better densification compared to lower pressure processes, e.g., [14,15];
- to allow the sintering beyond the thermal decomposition temperature by the condensation effect, i.e., pressure stabilizing structure (ex: MgB_2), e.g., [16];
- to sinter the high-pressure stable phase in the high-pressure stability domain (ex: c-C, c-BN), e.g., [17];
- to adjust the porosity, close to 0% (ex: transparent ceramics) or high porosity ($p > 50\%$) (ex: bone structure mimetic), e.g., [18];
- to increase the thermal stability of precursors by condensation effect by avoiding the departure of OH^- , H_2O , others volatile elements) [19];
- to decrease the sintering/consolidation/densification temperature by its driving force in order to avoid grain growth (which is always activated by high temperature), e.g., [20];
- to favor the structural phase existing only at lower temperature (ex for amorphous calcium phosphate), e.g., [21];

- to allow the consolidation of thermally unstable materials such as organic materials (ex: polymer) [22] and to allow the consolidation of composite constituted by materials of different thermal stability (ex: polymer composites) [23].

In this study, we therefore focus on the combination of high pressure (HP) with SPS, the technical developments and relevant results that have been made and obtained in the last decade. We will develop in more details the very new Ultra-High-Pressure (UHP)—SPS equipment and the promising results on the sintering of binderless polycrystalline diamond (binderless PCD) at very unexpected conditions highlighting the very high potential of this new technique compared to the classical PCD containing cobalt (Co-PCD) and their limited properties (Section 4).

2. Development of High Pressure SPS (HP-SPS) Using Conventional Equipment

Effect of pressure using conventional 1-stage assembly (Figure 1) was already observed despite the small range of pressure achievable with graphite mold (Figure 3) or higher pressure with much lower temperature using WC/Co mold (Figures 1 and 3) [24,25]. Typically, pressure decreases sintering temperature and therefore limits grain growth.

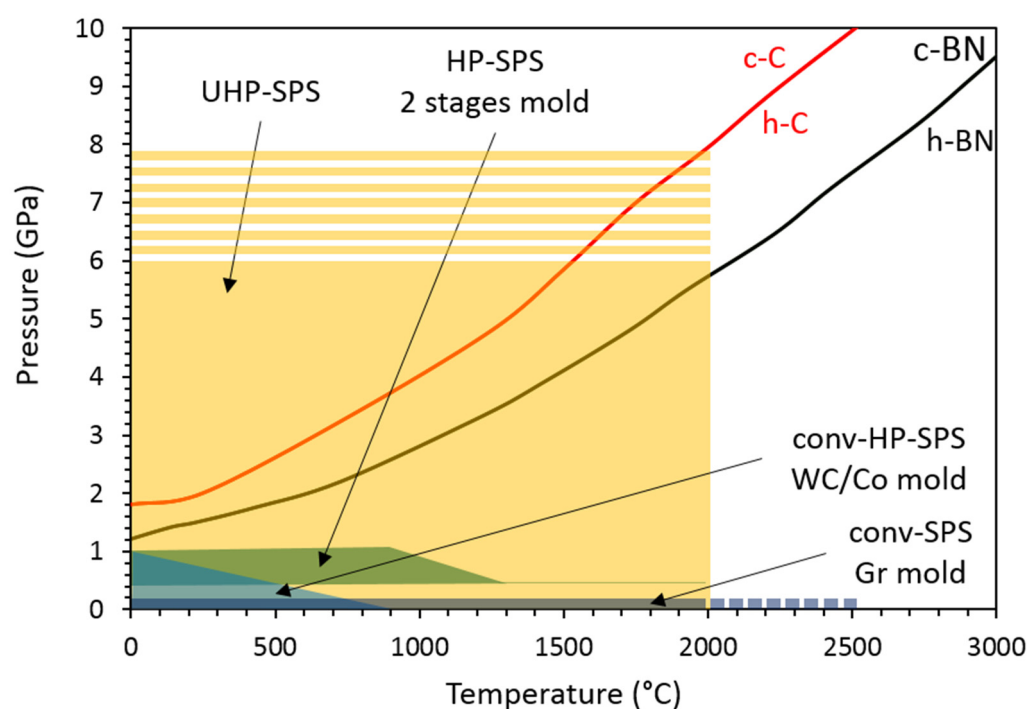


Figure 3. Pressure–temperature diagram showing field of applications of the different SPS setups. Conv-SPS and HP-SPS are both used in conventional equipment and never exceed 1 GPa. Maximum temperature depends a lot on materials constituting the mold, i.e., graphite, WC/Co, WC or SiC. In UHP-SPS equipment, a wide range of pressure–temperature conditions are covered offering the possibility to study sintering behavior of high-pressure phases such as c-C (red-curve) and c-BN (black curve) without any additions of binder.

In order to further inhibit grain growth during SPS process by reducing sintering temperature and therefore to keep a nano grains microstructure and enhance mechanical properties of materials due to Hall–Petch effect, some developments were made to perform high pressure experiments in conventional SPS equipment.

In 2006, the first double-stage SPS assembly was designed to perform experiments at pressure of up to 1 GPa and temperature to 930 °C [26] (Figure 3). Technical developments involved the use of an outer (1st stage) and inner (2nd stage) graphite stage (Figure 1). This outer graphite stage (heater shell) is used to ensure good heating rate. The other parts of the second stage consist of hard material pieces such as homemade binderless WC spacers and

SiC pistons. By using this double stage assembly, samples are very small, typically 5 mm in diameter and 1 to 3 mm thick. With this setup, it was shown that 95% relative density of fully stabilized zirconia is achieved at 900 °C at 1 GPa whereas 1400 °C is needed at 40 MPa. Therefore, this setup showed the efficiency of HP-SPS by keeping a microstructure with 10 nm grains at 1 GPa, 900 °C, whereas they grow to 200 nm at 40 MPa and 1400 °C. Similar setup was also used by replacing binderless WC protective discs by SiC ones [27] or simply by removing binderless WC discs [28] (Figure 1). In both cases, $P \sim 0.5$ GPa and temperature up to 1200 °C were reached (Figure 3), improving mechanical properties and transparency of sintered nano zirconia [27] and nano α -Al₂O₃ (corundum) [28]. Finally, other tests were performed by replacing inner graphite die by SiC ones [29–31]. With these modifications, sample diameter can reach 10 mm and still few mm thick. Again, maximum conditions are $P \sim 1$ GPa and 1000 °C whereas for lower pressure (0.4 GPa), temperature can be increased to 1300 °C (Figure 3), conditions that are sufficient to sinter nano grain transparent MgAl₂O₄ spinel [29,30] and α -Al₂O₃ [31].

Some other modifications of this pioneering double-stage assembly for HP-SPS in conventional equipment were proposed. In more details, SiC pistons were replaced by binderless WC ones [32–34] (Figure 1). Pressure and temperature conditions were not necessarily enhanced by these modifications and typically, maximum conditions were $P \sim 0.5$ GPa and 950–1000 °C even theoretically pressure of 1 GPa and temperature up to 1200 °C could be reached (Figure 3). In any of these studies, nano-grained transparent materials are obtained.

However, by comparing these two types of pistons, the question about the heating and current pathways aroused. It is of note that no information is given about the structure of the SiC used (α vs. β) which asks the questions whether there are conductive or insulators and that therefore if current passes through the powders (SPS principle)

Indeed, electrical resistivity of SiC is about 8–9 order of magnitude higher than that of binderless WC, 10^2 – 10^3 Ω m and 2.0×10^7 Ω m, respectively [32]. This would imply that using SiC pistons and/or discs, samples would be electrically isolated, that heating would occur by resistive heating of the outer and inner graphite dies and that the spark effect of the SPS process would not occur between grains. Sintering would therefore occur by hot pressing (Figure 3). However, the use of binderless WC pistons and discs allows the current to be injected inside the sample powder and the SPS process is effective. Moreover, heating is not only ensured by the graphite dies but also by the pistons. Additionally, to reach higher temperature at relatively high pressure, low-cost carbon fiber composite (CFC) pistons were also developed and allow to reach 2000 °C at 0.4 GPa [34] (Figure 3).

To summarize, HP-SPS double stage assemblies using conventional equipment were essentially developed in order to decrease sintering temperature and therefore keep a nano-grain microstructure that enhance strengthening of materials due to the presence of high density of grain boundaries, so called Hall–Petch effect. However, by using these double stage assemblies with always an outer graphite die, pressure and temperature are limited to 1 GPa and 1000 °C, respectively (Figure 3). Moreover, materials used as pistons asked the question of real SPS process inside the samples (Figure 1). There is therefore a real lock to overpass with the development new material molds with significant electrical conductivity and also high mechanical properties that would allow to work at both high-pressure high temperature and also under air conditions instead of vacuum. Finally, in order to consider sintering by SPS of very hard materials such as diamond and c-BN, higher pressure and temperature are mandatory and new equipment have to be developed (Section 3).

3. Recent Developments: UHP-SPS

Based on the respective advantages of high pressure and spark plasma sintering, i.e., lowering temperature and faster conditions of sintering as well as the stabilization of high-pressure phases, two experimental setups were recently designed to couple Ultra-High-Pressure apparatus (UHP) and Spark plasma sintering (SPS), a process so-called UHP-SPS that can reach up to 6 to 8 GPa and 2000 °C (Figure 3).

Two different groups were coupled with ultra-high pressure (UHP) with SPS in the past 5 years. In both groups, a large volume press was used with their typical assembly. The main difference with conventional 1- or 2-stage SPS is that in large volume press assembly, furnaces use thin wall graphite, metals or LaCO_3 , whereas the whole mold is the furnace in conventional SPS equipment (1- and 2-stage) (Figure 1). Therefore, less energy is needed to heat these thin wall furnaces compared to large molds. It is also of note that no vacuum is needed by using these UHP-SPS setups contrary to conventional SPS and HP-SPS in conventional equipment. Indeed, contrary to conventional SPS or even HP-SPS using graphite dies, graphite furnace and spacers in UHP-SPS are never in contact with air but enclosed in ceramic pressure transmitting medium and during the process no oxygen is available.

The first group, from the University of Krakow, Poland, coupled a Bridgman type toroid large volume press and a homemade 50 Hz alternating or 1 kHz pulsed current injected inside the sample thanks to an adapted designed assembly (Figure 1) [35–37]. Typically, assembly consists of a pressure transmitting medium (ceramic) in which a graphite furnace is inserted in which sample (15 mm diameter and 5 mm thickness) is loaded at the center. Sleeves and spacers are typically used to improve good hydrostaticity and the specificity here is that graphite spacers are inserted at the top and bottom of the sample and in contact with the furnace to allow the current to be injected in the sample and therefore create and use the SPS process (Figure 1). Using this setup, very refractory phases were sintered and the combine effect of pressure and SPS allows to decrease sintering temperature and time, and therefore maintain a nano-grain structure with enhanced mechanical properties [35,36]. Another study compared classic HP-HT (sample electrically isolated) and UHP-SPS of diamond- TiB_2 composite under similar conditions of pressure and temperature [37]. Due to the advantages of SPS, diamond remains stable whereas it destabilizes to graphite using classic HP-HT [37], making UHP-SPS a promising tool to sinter high pressure phases even at metastable/unequilibrium conditions.

The second group, from the University of Bordeaux, France, associated a Belt-type large volume press and a conventional electric pulsed current source from Fuji Electronic Industrial (model SCM-3000) that can reach 3000 A for 10 V with a pulse duration of 3 ms. Details on the press design and current source as well as calibration are available in [38]. Assembly is an external pressure transmitting medium in fired pyrophyllite in which a graphite furnace is inserted (Figure 1). Sample powder (maximum 17 mm diameter and 10 mm thickness) is loaded directly in contact with the furnace or surrounded by a sleeve, mostly in h-BN (Figure 1). Powder is directly in contact with graphite punches to allow the injection of current (Figure 1). By using this setup, it has been shown that the direct conversion sintering of $\gamma\text{-Al}_2\text{O}_3$ to $\alpha\text{-Al}_2\text{O}_3$ occurred at much lower temperature than is classic HP-HT setup, for example at 500 °C and 800 °C at 1.5 GPa [12,38,39]. This setup was also used for the joining/consolidation of drilling bits at high pressure temperature by joining WC/Co substrate tables by polycrystalline diamond compact (PDC: Diamond/Co and pure diamonds) [38]. In both cases, sintering occurred at lower temperature than in classic HP-HT setups. Another example showed the sintering of MgB_2 [16]. Here, the increase in pressure (in the range 2 to 5 GPa) stabilized the phase above its decomposition temperature and high temperature promoted the sintering up to relative density of 100% with a fine-grain microstructure [16].

These two setups were compared with conventional SPS for the sintering of $\beta\text{-SiC}$ [40]. No obvious difference was observed between the two UHP-SPS setups. However, it is clear that the high pressure promotes the densification at lower temperature, therefore limiting diffusion and associated grain growth that could occur in conventional SPS due to the very high temperature of sintering ($T \sim 1800$ °C) [40].

A final attempt was to use cubic-type multi-anvil press with an adapted assembly to allow an AC current to be injected inside the sample [41]. In this way, pure Mo sintering was achieved up to 98.5% at 9 GPa, 1300 °C and for 1 min [41]. Pressure is the main parameter to obtain highly dense materials and injection of current inside the samples has

a benefit effect on hardness and bending strength, as well as on limited grain growth due to the fast process [41].

4. Application to Binderless Diamond Sintering

4.1. Brief History of Binderless Diamond Sintering

Since the first synthesis of diamonds in the mid-50s, early 60s [10,11], a lot of setups were developed to sinter diamonds and fabricate bulk objects. In the 70s, polycrystalline diamond compacts (PDC) were processed with the help of a metallic binder [42]. Briefly, the principle is to synthesis diamond particles from graphite that is mixed with a metallic catalyzer (mostly Ni). At 4–5 GPa, 1300–1400 °C, graphite transforms to diamonds grains [43]. After recovery and different steps of leaching, these diamond grains are sintered at HP-HT using a Cobalt binder to make these PCD that are typically mounted on WC/Co supports to fabricate PDC [42]. Due to their good mechanical properties, these objects are used for cutting and drilling tools. However, above 400 °C, these objects deteriorate quite easily due to heating by friction [44].

In order to overcome this issue, to reach higher mechanical properties with higher life duration tools and also to use other diamond aspects such as its optical or thermal properties, binderless diamond sintering has been developed almost 20 years ago from the pioneering work of Voronov (2000) and Irifune et al. (2003) [45,46].

A wide literature exists on binderless diamonds sintering and a recent review has also been published [47]. Therefore, in the following, a brief summary is given concerning the technical development, the physical process to sinter these objects and their associated physical properties.

Typically, there are two methods to sinter binderless diamonds using High Pressure—High Temperature (HP-HT) techniques. In both methods, quasi-hydrostatic pressure is generated using a specific hydraulic press called a multi anvil apparatus (MAA) that can generate very high pressure (several tens of GPa typically) on large samples (few mm³) due to their multi-stage assemblies. Temperature is typically generated using resistive heating furnaces in graphite or metals thanks to a high-power power supply. Finally, samples are thermally isolated from the furnace using specific materials.

The first method was jointly developed in Japan by Geodynamics Research Center (GRC) and Sumitomo Electric Industry (SEI), represented by Pr. T. Irifune and Dr. H. Sumiya, respectively, and consists of Direct Conversion Sintering (DCS) of graphite [46,48–55] or other pure carbon sources [49,51,56] to diamond objects. In order to obtain an object of ~1 cm³, dedicated Kawai multi-anvil press was developed [57]. Typically, DCS occurs for diamond at $P > 15 \text{ GPa}$ and $2000 \text{ °C} < T < 2500 \text{ °C}$ and final products are yellowish (due to the presence of nitrogen) transparent Nano-Polycrystalline Diamond (NPD) compact. According to the P-T conditions and carbon source, Lonsdaleite, another high-pressure phase of carbon, and lamellae structures are more or less observed, that can modify physical properties of the NPD [49,51]. Typically, NPD have exceptional mechanical properties (Young's modulus, hardness, wear rate ...) that highly exceed those of PDC and even those of natural diamonds single crystal [50]. Optical and thermal properties are also exceptional and similar to those of natural single crystal [58]. Therefore, NPD are the perfect tools that can replace PDC and natural single crystal for cutting/drilling tools, optical windows and thermal sink. However, the very high P-T conditions and very specific equipment make the industrial transfer impossible and up to now, applications are essentially dedicated to scientific areas [59].

The second method tries to decrease sintering conditions of binderless diamonds using directly diamonds powders. This protocol was first trialed by Hall, 1970 [17] who argued that diamond powders can be sintered at high pressure-high temperature. The degree of sintering depends on P, T, t pathways as well as on starting grain size [17], an idea that was developed later with the addition of the nature of precursors (natural, HPHT and detonation diamonds) [45,60,61]. However, sintered objects were never fully dense, and some back transformation occurred due to the limited P-T conditions reached in

their respective apparatus (piston-cylinder and belt-type press). This method was further developed by the University of Sichuan, China [62–66]. An optimized cubic hinge-type apparatus was used to sinter objects up to 0.5 cm^3 at pressure up to 16 GPa and temperature to 2500°C [62]. Fully dense diamond objects, called CF-PDC or MPD for Catalyst-free Polycrystalline Diamonds compact or Microcrystalline Polycrystalline Diamond, can be obtained at pressure and temperature down to 14 GPa and 1500°C , respectively [63–66]. However, samples that present micro-cracks are black translucent, and TEM observations revealed the presence of a very small amount of graphite at triple junctions [63–65]. Despite these features, hardness of CF-PDC or MPD are similar to those of NPD and present a high thermal stability, but the optical properties are not very useful [63–65].

4.2. UHP-SPS Setup with Belt-Type HP Apparatus for the Sintering of Diamond Powders

One of the main goals to couple UHP and SPS is to sinter high pressure phases at unexpected conditions of pressure and temperature (Figure 3) without the use of any binder to ensure exceptional physical properties (mechanical, optical, electrical and thermal). In this aim, one can site the sintering of very hard materials such as c-BN and diamonds (c-C) that are stable at pressure well above those achievable by conventional SPS and 2-stage HP-SPS, i.e., limited to maximum pressure of 1 GPa. As described above, these two materials are sintered at minimum pressure of 8–9 GPa for c-BN and 12 GPa for diamonds using multi-anvil devices and by resistive heating [52,67,68].

Here, sintering of binderless diamonds were performed using two different grain sizes of commercial diamonds from the company Pureon. These powders are synthetic diamonds produced by HP-HT techniques using metallic catalyst and purified by chemical treatments (MSY grade, purity > 99%) and grain sizes were precisely controlled and are $0.75\text{--}1.25 \mu\text{m}$ and $8\text{--}12 \mu\text{m}$ with a narrow grain size distribution. XRD show only sharp diamond peaks, typical of very well crystallized powders (Figure 4). SEM images show automorph grains, and average grain sizes correspond to those provided by the supplier. (Figure 5).

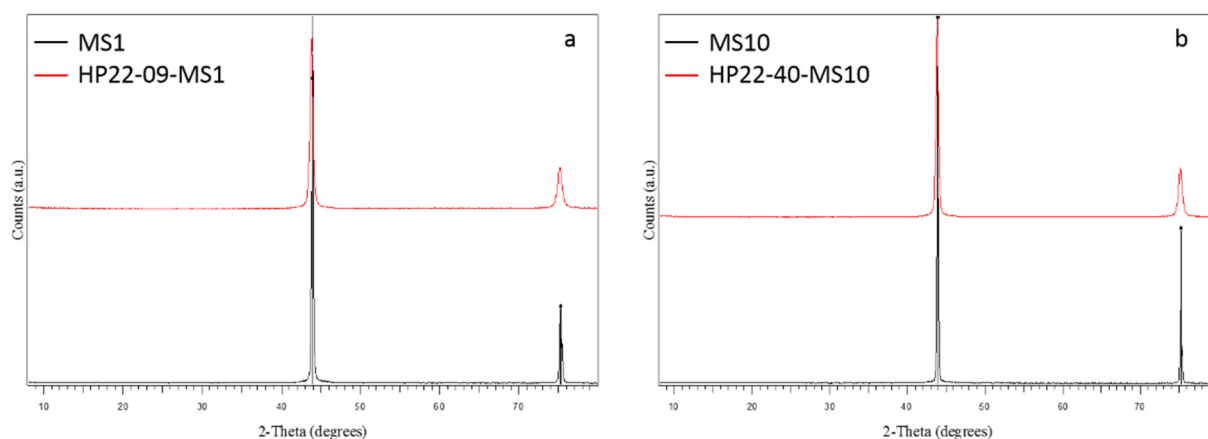


Figure 4. XRD patterns of starting materials (black) and run products after experiments (red): (a) For the experiments conducted with $0.75\text{--}1.25 \mu\text{m}$ grain size powder and (b) with $8\text{--}12 \mu\text{m}$ grain size powder. The starting powders are very pure, and grains are well crystallized (sharp peaks). After experiment, diamond is fully conserved with no evidence of graphite back transformation. It is of note that diffraction peaks in experimental products are wider than in the starting powder.

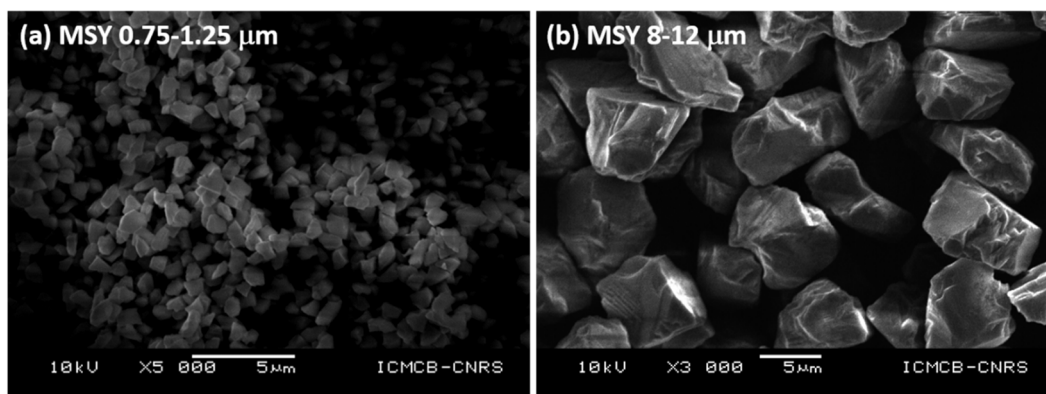


Figure 5. SEM images (SEI mode, 10 kV, WD = 10 mm) of the starting powders: (a) 0.75–1.25 μm grain size and (b) 8–12 μm grain size.

For each run, about 0.5 g of diamond powder was packed in the UHP-SPS assembly. It is of note that for contamination/pollution purpose, powders were not packed directly in contact with the graphite furnace and papyex sheets. For this purpose, a sleeve of h-BN and two Mo discs are placed at the top and bottom of the powder (Figure 1). This reduces the sample size to 11 mm in diameter and 2–3 mm in thickness (Figures 1 and 6c,d).

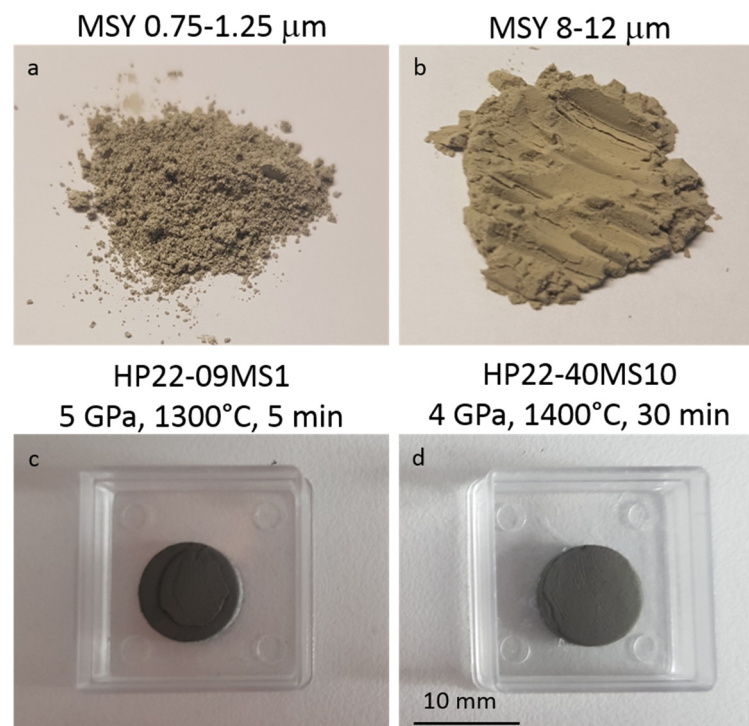


Figure 6. Macroscopic view of starting materials (a,b), with grain size 0.75–1.25 μm (a) and 8–12 μm (b), respectively. Starting powders are yellowish. Bottom row shows recovered samples after experiments at HP-HT using our UHP-SPS setup and powders described above (c,d). Recovered samples are solid discs of 11 mm diameter and 2–3 mm thickness.

For each run, pressure is first increased to the target in 30 to 45 min using calibration made on the variation of resistance of different pressure metal calibrant that experienced phase transition at a given pressure [38]. Then, temperature is increased to the target based on the previous calibration made on the melting point of temperature metals calibrant at 4 GPa [38]. Heating rate is typically 100 $^{\circ}\text{C}/\text{min}$, using a SPS pulsed current of 3.3 ms and a ON:OFF sequence of 12:2. Dwell times were varied from 1 to 30 min and decompression

was also varied from 30 min to several hours (overnight) (Figure 7a). During the whole process, anvil displacement is recorded first for follow powder densification and also to ensure that there is no contact between anvils and WC/Co die (chamber, cylinder, ring) (Figure 7b).

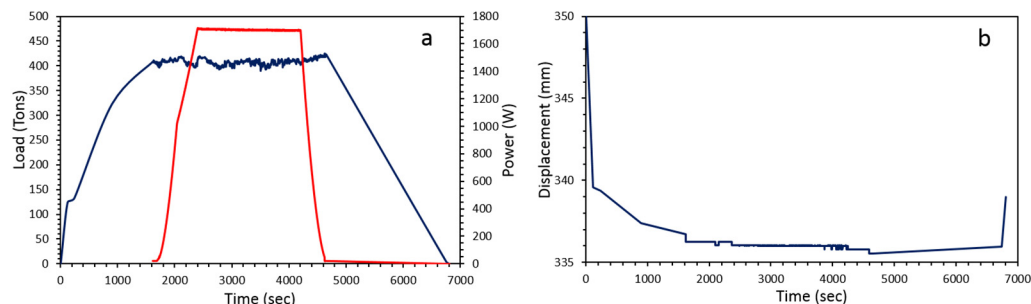


Figure 7. (a) Load (tons, in blue) and power (W, in red) parameters as programmed and recorded during experiments and associated displacement in mm (b). During dwell, both load and power, i.e., pressure and temperature, are very stable. Most of the displacement occurs during cold compression (few mm) whereas it is only of few tens to hundreds of microns during heating and dwell.

Two experiments are presented in the following. Run HP22-09-MS1 was performed using 0.75–1.25 μm powder loaded at 5 GPa and heated to 1300 $^{\circ}\text{C}$ for 5 min and run HP22-40-MS10 was carried out 8–12 μm powder at 4 GPa and 1400 $^{\circ}\text{C}$ for 30 min (Table 1, Figures 4, 6, 8 and 9).

Table 1. Experimental conditions and main results.

Run #	Grain Size (μm)	Quantity (g)	P (GPa)	T ($^{\circ}\text{C}$)	Dwell Time (min)	¹ Density (g cm^{-3})	XRD	Grain Boundary Formation
HP22-09-MS1	0.75–1.25	0.5	5	1300	5	3.05	c-C	+++
HP22-40-MS10	8–12	0.5	4	1400	30	2.80	c-C	++

¹ Density measured by Archimedes' method.

After experiment bulk samples were recovered as solid discs of ~ 11 mm diameter and 2–3 mm thick (no mass loss and no color change was observed compared to the starting powders (Figure 6)). Although experiments were performed at the limit or out of the diamond stability field, for both recovered samples, XRD patterns show only diamond peaks with no evidence of destabilization into graphite or more amorphous sp^2 forms (Figure 4). The only difference with XRD of the starting powders is that diffraction peaks are wider after experiments (Figure 4). It is unlikely to be due to a grain size reduction during experiments as shown on SEM images where no or little grain fracturation and grounding are observed (Figures 8 and 9). Therefore, it is most likely to be due to residual stress inside grains after experiments.

Sample density was measured using the Archimedes method. It is found that HP22-09-MS1 has a density slightly higher than HP22-40-MS10 at 3.05 g cm^{-3} and 2.80 g cm^{-3} , respectively, corresponding to a relative density of 87 and 79% or a porosity of 13 and 21%. This suggest that is easier to sinter small grain size powder of around 1 micron than a bigger grain size around 10 microns. Despite this relative low density, samples are very mechanically resistant. It is of note that density can be improved by mixing different sizes of diamond powder and plays on the P, T, t pathway.

These compacts, which were not fully dense, were selected to show better images of the neck formation between the grains. SEM observations using a JEOL-6360A (SEI mode, 10–15 kV, WD = 10 mm) at low magnification ($\times 2000$) show different areas more or less densified inside both samples (Figures 8a and 9a,b). Indeed, it is clearly visible that some areas are “only” compacted powders whereas others show sintered structures.

This suggests that there is a kind of heterogeneity inside the samples. This could be due to local thermal/pressure gradient during the sintering process and/or that conditions of duration are not optimized to fully densified samples. It is also observed that there are more dense areas in samples sintering with $0.75\text{--}1.25\ \mu\text{m}$ grains (Figure 8a) than in the $8\text{--}12\ \mu\text{m}$ grains (Figure 9a,b), explaining the difference in the measured density (Table 1). At higher magnification ($\times 5000$ and $\times 10,000$), grains are more visible, no grain fracturation is observed in both samples and 1-micron grains have still sharp edges compared to starting powder, whereas those of 10-microns grains are smoother than in the starting powder. Moreover, two different types of microstructures are clearly present in both samples (Figure 8b,c and Figure 9c–e). On one hand, samples are composed of compacted grains, i.e., as a green body. On the other hand, the denser areas in both samples show the formation of grain boundaries between grains (Figure 8b,c and Figure 9c–e) at very unexpected pressure-temperature conditions. These dense areas are more present and in samples containing 1-micron grains (Figure 8b,c, HP22-09MS1) than in 10-microns grain sample (Figure 9c–e, HP22-40-MS10). Indeed, in the former case (1-micron grains) hundreds to thousands of grains could be sintered together forming these large dense areas (Figure 8b) whereas in the latter case (10-micron grains), only few grains are sintered together (Figure 9c–e). It of note that small powder grain sizes were sintered at higher pressure (5 GPa) and lower temperature ($1300\ ^\circ\text{C}$) and for shorter duration (5 min) than the bigger powder grain size (4 GPa, $1400\ ^\circ\text{C}$, 30 min). This indicates that pressure is of main importance in the sintering process and that smaller grain size diamond powder are easier to sinter compared to bigger ones. It could therefore be very interesting to sinter nanodiamonds at similar conditions to improve densification. However, as sintering conditions are close or even out of the stability field of diamonds, there is subtle balance to consider between powder grain size, its reactivity and P-T conditions.

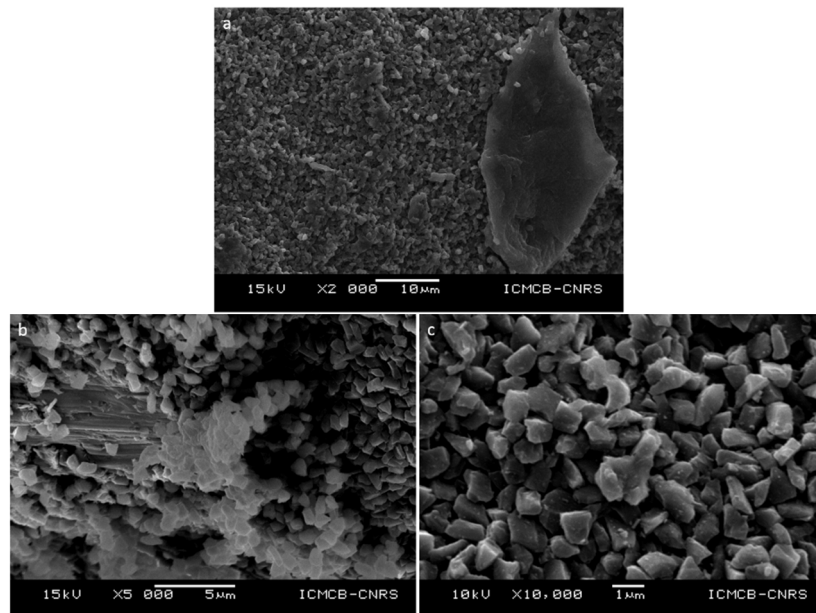


Figure 8. Microstructure of HP22-09-MS1 recovered sample observed in SEM (SEI, 15 kV, WD = 10 mm) at different magnification ((a) $\times 2000$, (b) $\times 5000$ and (c) $\times 10,000$). First, there is no evidence for grain fracturation, nor the presence of other phases. There are two types of regions inside the samples (a,b), typically more or less sintered suggesting that densification is heterogeneous and not total (a–c). In more densified areas, a lot of grain boundaries are observed (b) whereas grains are only packed in less densified areas with only few grains that can be sintered (center of (c) for example).

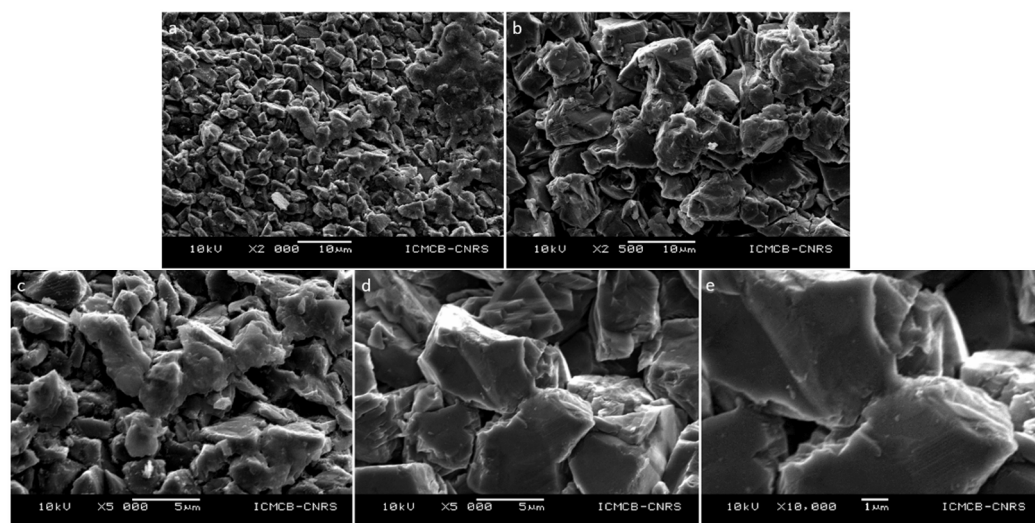


Figure 9. Microstructure of HP22-40-MS10 recovered sample observed in SEM (SEI, 10 kV, WD = 10 mm) at different magnification ((a) $\times 2000$, (b) $\times 2500$, (c,d) $\times 5000$ and (e) $\times 10,000$). There is no evidence for grain fracturation, nor the presence of other phases. Due to larger grain size, there are less areas sintered (a,b). However, in these areas, it is evident that grains boundaries are formed or in the process of formation (c–e).

These results show that, by combining high pressure apparatus and SPS, the sintering of high-pressure phases such as binderless diamonds could be achieved at much lower conditions than those previously conducted by conventional HP-HT apparatus. This opens a new field in material sciences for the very hard materials sintering and the stabilization of high-pressure phases.

5. Conclusions

Conventional SPS has been used for decades for the sintering of very different materials such as metals, ceramics or composites. The main advantages of this technique are twofold. The high temperature is reached quickly and the current injection inside the powder allows a fast densification of samples. Thus, grain growth is inhibited, and grain size remains relatively small, improving materials properties.

With the aim to further enhance these properties, HP-SPS setup has been developed to be adapted in conventional equipment. Two-stage assemblies with hard materials pistons (in SiC or pure WC) increase pressure conditions to 1 GPa but temperature cannot exceed 1000 °C and sample sizes are also limited to few mm in diameter and thickness. However, the high pressure has the effect to reduce the sintering temperature and therefore samples with nano-grains (few nm to few tens of nm) microstructure were obtained. Recovered samples have typically better mechanical and optical properties than those sintered by conventional SPS.

The recent developments of UHP-SPS equipment with dedicated large volume press (Bridgman or Belt-type apparatus) allows reaching 6 to 8 GPa and up to 2000 °C. Such high pressure still decreases sintering temperatures and coupling with SPS yields similar results compared to classic HP-HT. Moreover, such high pressures allow to stabilize phases with low temperature destabilization and also promote the densification of high pressure phases such c-C without any binder at very unexpected conditions. Indeed, we have shown that microcrystalline diamond powders (0.75–1.25 and 8–12 μm) could be sintered at 4–5 GPa and temperature between 1300 and 1400 °C. Although samples are not fully dense, observation of grain boundary formation highlight the sintering process at P-T conditions out of diamond equilibrium. Some improvements can be made to obtain fully dense materials such as dwell duration, heating, cooling and decompression rate, mixing of different grain size powders and probably the on/off sequence. UHP-SPS is thus a

promising tool that could be applied to a lot of different hard materials such as c-BN or other borides, nitrides, carbides and even hard ceramics and composites.

Finally, environmental fingerprints are reduced by using these high pressure SPS sintering because they consume less electrical energy and materials obtained have better properties providing them a high life duration.

Author Contributions: J.G. contributed to investigation, formal analysis, data curation, validation and writing—original draft preparation. M.P. contributed to conceptualization, supervision, editing, formal analysis and project co-administration. A.L. contributed to conceptualization, methodology, investigation, resources, supervision, writing—review and editing and project administration. All authors have read and agreed to the published version of the manuscript.

Funding: The authors thank CNRS prématuration project DiamCeram (prematuration 2020/AL 12 20) for funding this study.

Institutional Review Board Statement: Not applicable.

Informed Consent Statement: Not applicable.

Data Availability Statement: Not applicable.

Acknowledgments: The authors thank Stéphane TOULIN (ICMCB, UMR5026) for providing us with assistance with bibliography, Corinne MONNIER (CNRS INNOVATION) and Paola TORRES (CNRS, DR15) for their efficient and helpful contribution.

Conflicts of Interest: The authors declare no conflict of interest.

References

1. Inoue, K. Electric Discharge Sintering. U.S. Patent No. 3,241,956, 22 March 1966.
2. Inoue, K. Apparatus for Electrically Sintering Discrete Bodies. U.S. Patent No. 3,250,892, 10 May 1966.
3. Grasso, S.; Sakka, Y.; Maizza, G. Electric current activated/assisted sintering (ECAS): A review of patents 1906–2008. *Sci. Technol. Adv. Mater.* **2009**, *10*, 053001. [[CrossRef](#)] [[PubMed](#)]
4. Tokita, M. Progress of Spark Plasma Sintering (SPS) Method, Systems, Ceramics Applications and Industrialization. *Ceramics* **2021**, *4*, 160–198. [[CrossRef](#)]
5. Guignard, J.; Bystricky, M.; Béjina, F. Dense fine-grained aggregates prepared by spark plasma sintering (SPS), an original technique in experimental petrology. *Eur. J. Miner.* **2011**, *23*, 323–331. [[CrossRef](#)]
6. Chaim, R. Densification mechanisms in spark plasma sintering of nanocrystalline ceramics. *Mater. Sci. Eng. A* **2007**, *443*, 25–32. [[CrossRef](#)]
7. Chaim, R.; Marder, R.; Estournés, C.; Shen, Z. Densification and preservation of ceramic nanocrystalline character by spark plasma sintering. *Adv. Appl. Ceram.* **2012**, *111*, 280–285. [[CrossRef](#)]
8. Demuynck, M.; Erauw, J.-P.; Van der Biest, O.; Delannay, F.; Cambier, F. Densification of alumina by SPS and HP: A comparative study. *J. Eur. Ceram. Soc.* **2012**, *32*, 1957–1964. [[CrossRef](#)]
9. Demazeau, G. High Pressure and Chemical Bonding in Materials Chemistry. *Zeit. Nat. B* **2006**, *61*, 799–807. [[CrossRef](#)]
10. Liander, H.; Lundald, E. Some observations on the synthesis of diamonds. *Ark. Kemi* **1961**, *16*, 139–149.
11. Bundy, F.P.; Hall, H.T.; Strong, H.M.; Wentorf, R.H., Jr. Man-made diamonds. *Nature* **1955**, *176*, 51–55. [[CrossRef](#)]
12. Liao, S.-C.; Chen, Y.-J.; Kear, B.H.; Mayo, W.E. High pressure/low temperature sintering of nanocrystalline alumina. *Nanostruct. Mater.* **1998**, *10*, 1063–1079. [[CrossRef](#)]
13. Liao, S.-C.; Chen, Y.-J.; Mayo, W.E.; Kear, B.H. Transformation-assisted consolidation of bulk nanocrystalline TiO₂. *Nanostruct. Mater.* **1999**, *11*, 553–557. [[CrossRef](#)]
14. Ma, D.; Kou, Z.; Liu, Y.; Wang, Y.; Gao, S.; Luo, X.; Li, W.; Wang, Y.; Du, Y.; Lei, L. Sub-micron binderless tungsten carbide sintering behavior under high pressure and high temperature. *Int. J. Refract. Met. Mater.* **2016**, *54*, 427–432. [[CrossRef](#)]
15. Gao, J.; Wang, D.; Lei, L.; Zhang, F.; Zhang, J.; Fu, Z. High-pressure Sintering of Boron Carbide-Titanium Diboride Composites and Its Densification Mechanism. *Adv. Mater.* **2020**, *35*, 356–362. [[CrossRef](#)]
16. Prakasam, M.; Balima, F.; Noudem, J.; Largeteau, A. Dense MgB₂ Ceramics by Ultrahigh Pressure Field-Assisted Sintering. *Ceramics* **2020**, *3*, 521–532. [[CrossRef](#)]
17. Hall, H.T. Sintered Diamond: A Synthetic Carbonado. *Science* **1970**, *169*, 868–869. [[CrossRef](#)] [[PubMed](#)]
18. Wang, J.; Shaw, L.L. Transparent nanocrystalline hydroxyapatite by pressure-assisted sintering. *Scr. Mater.* **2010**, *63*, 593–596. [[CrossRef](#)]
19. Nisr, C.; Chen, H.; Leinenweber, K.; Chizmeshya, A.; Prakapenka, V.B.; Prescher, C.; Tkachev, S.N.; Meng, Y.; Liu, Z.; Shim, S.-H. Large H₂O solubility in dense silica and its implications for the interiors of water-rich planets. *Proc. Natl. Acad. Sci. USA* **2020**, *117*, 9747–9754. [[CrossRef](#)]

20. Liu, L.; Li, X.; He, Q.; Xu, L.; Cao, X.; Peng, X.; Meng, C.; Wang, W.; Zhu, W.; Wang, Y. Sintering dense boron carbide without grain growth under high pressure. *J. Am. Ceram. Soc.* **2018**, *101*, 1289–1297. [[CrossRef](#)]
21. Rubenis, K.; Zemjane, S.; Vecstaudza, J.; Bitenieks, J.; Locs, J. Densification of amorphous calcium phosphate using principles of the cold sintering process. *J. Eur. Ceram. Soc.* **2021**, *41*, 912–919. [[CrossRef](#)]
22. Sébilleau, J.-C.; Lemonnier, S.; Barraud, E.; Vallat, M.-F.; Carradò, A.; Nardin, M. Effects of pressure on poly(ether-ether-ketone) (PEEK) sintering mechanisms. *J. Appl. Polym. Sci.* **2019**, *136*, 47645. [[CrossRef](#)]
23. Adesina, O.T.; Sadiku, E.R.; Adesina, O.S.; Ogunbiyi, O.F.; Jamiru, T.; Obadele, B.A. Spark plasma sintering of polymer and polymer-based composites: A review. *Int. J. Adv. Manuf. Technol.* **2021**, *116*, 759–775. [[CrossRef](#)]
24. Munir, Z.A.; Anselmi-Tamburini, U.; Ohyanagi, M. The effect of electric field and pressure on the synthesis and consolidation of materials: A review of the spark plasma sintering method. *J. Mater. Sci.* **2006**, *41*, 763–777. [[CrossRef](#)]
25. Hungria, T.; Galy, J.; Castro, A. Spark Plasma Sintering as a Useful Technique to the Nanostructuration of Piezo-Ferroelectric Materials. *Adv. Eng. Mater.* **2009**, *11*, 615–631. [[CrossRef](#)]
26. Anselmi-Tamburini, U.; Garay, J.E.; Munir, Z.A. Fast low-temperature consolidation of bulk nanometric ceramic materials. *Scr. Mater.* **2006**, *54*, 823–828. [[CrossRef](#)]
27. Zhang, H.B.; Kim, B.-N.; Morita, K.; Yoshida, H.; Lim, J.-H.; Hiraga, K. Optimization of high-pressure sintering of transparent zirconia with nano-sized grains. *J. Alloys Compd.* **2010**, *508*, 196–199. [[CrossRef](#)]
28. Ghanizadeh, S.; Grasso, S.; Ramanujam, P.; Vaidhyanathan, B.; Binner, J.; Brown, P.; Goldwasser, J. Improved transparency and hardness in α -alumina ceramics fabricated by high-pressure SPS of nanopowders. *Ceram. Int.* **2017**, *43*, 275–281. [[CrossRef](#)]
29. Sokol, M.; Kalabukhov, S.; Dariel, M.P.; Frage, N. High-pressure spark plasma sintering (SPS) of transparent polycrystalline magnesium aluminate spinel (PMAS). *J. Eur. Ceram. Soc.* **2014**, *34*, 4305–4310. [[CrossRef](#)]
30. Sokol, M.; Halabi, M.; Mordekovitz, Y.; Kalabukhov, S.; Hayun, S.; Frage, N. An inverse Hall-Petch relation in nanocrystalline MgAl_2O_4 spinel consolidated by high pressure spark plasma sintering (HPSPS). *Scr. Mater.* **2017**, *139*, 159–161. [[CrossRef](#)]
31. Ratzker, B.; Wagner, A.; Sokol, M.; Kalabukhov, S.; Dariel, M.P.; Frage, N. Optical and mechanical properties of transparent alumina fabricated by high-pressure spark plasma sintering. *J. Eur. Ceram. Soc.* **2019**, *39*, 2712–2719. [[CrossRef](#)]
32. Grasso, S.; Kim, B.-N.; Hu, C.; Maizza, G.; Sakka, Y. Highly Transparent Pure Alumina Fabricated by High-Pressure Spark Plasma Sintering. *J. Am. Ceram. Soc.* **2010**, *93*, 2460–2462. [[CrossRef](#)]
33. Eriksson, M.; Liu, Y.; Hu, J.; Gao, L.; Nygren, M.; Shen, Z. Transparent hydroxyapatite ceramics with nanograin structure prepared by high pressure spark plasma sintering at the minimized sintering temperature. *J. Eur. Ceram. Soc.* **2011**, *31*, 1533–1540. [[CrossRef](#)]
34. Grasso, S.; Yoshida, H.; Porwal, H.; Sakka, Y.; Reece, M. Highly transparent α -alumina obtained by low cost high pressure SPS. *Ceram. Int.* **2013**, *39*, 3243–3248. [[CrossRef](#)]
35. Yung, D.-L.; Cygan, S.; Antonov, M.; Jaworska, L.; Hussainova, I. Ultra high-pressure spark plasma sintered ZrC-Mo and ZrC-TiC composites. *Int. J. Refract. Met. Hard Mater.* **2016**, *61*, 201–206. [[CrossRef](#)]
36. Knaisslová, A.; Novák, P.; Cygan, S.; Jaworska, L.; Cabibbo, M. High-Pressure Spark Plasma Sintering (HP SPS): A Promising and Reliable Method for Preparing Ti–Al–Si Alloys. *Materials* **2017**, *10*, 465. [[CrossRef](#)] [[PubMed](#)]
37. Jaworska, L.; Karolus, M.; Cygan, S.; Morgiel, J.; Cyboron, J.; Łukasik, J.L.; Putyra, P. Influence of pulsed current during high pressure sintering on crystallite size and phase composition of diamond with Ti-B bonding phase. *Int. J. Refract. Met. Hard Mater.* **2018**, *70*, 101–106. [[CrossRef](#)]
38. Balima, F.; Bellin, F.; Michau, D.; Viraphong, O.; Poulon-Quintin, A.; Chung, U.-C.; Dourfaye, A.; Largeteau, A. High pressure pulsed electric current activated equipment (HP-SPS) for material processing. *Mater. Des.* **2018**, *139*, 541–548. [[CrossRef](#)]
39. Balima, F.; Largeteau, A. Phase transformation of alumina induced by high pressure spark plasma sintering (HP-SPS). *Scr. Mater.* **2019**, *158*, 20–23. [[CrossRef](#)]
40. Prakasam, M.; Balima, F.; Cygan, S.; Klimczyk, P.; Jaworska, L.; Largeteau, A. Ultrahigh pressure SPS (HP-SPS) as new syntheses and exploration tool in materials science. In *Spark Plasma Sintering: Current Status, New Developments and Challenges*; Elsevier: Amsterdam, The Netherlands, 2019; Chapter 9; pp. 201–218. [[CrossRef](#)]
41. Zhou, Z.; Deng, N.; Wang, H.; Du, J. Fabrication of fine grained molybdenum by fast resistance sintering under ultra-high pressure. *J. Alloys Compd.* **2019**, *782*, 899–904. [[CrossRef](#)]
42. Katzman, H.; Libby, W.F. Sintered Diamond Compacts with a Cobalt Binder. *Science* **1971**, *172*, 1132–1134. [[CrossRef](#)]
43. Strong, H.M.; Hanneman, R.E. Crystallization of Diamond and Graphite. *J. Chem. Phys.* **1967**, *46*, 3668–3676. [[CrossRef](#)]
44. Westraadt, J.E.; Sigalas, I.; Neethling, J.H. Characterisation of thermally degraded polycrystalline diamond. *Int. J. Refract. Met. Hard Mater.* **2015**, *48*, 286–292. [[CrossRef](#)]
45. Voronov, O.; Tompa, G.; Sadangi, R.; Kear, B.; Wilson, C.; Yan, P. *Superhard Nanophase Cutter Materials for Rock Drilling Applications*; Diamond Materials Inc.: Piscataway, NJ, USA, 2000. [[CrossRef](#)]
46. Irifune, T.; Kurio, A.; Sakamoto, S.; Inoue, T.; Sumiya, H. Ultrahard polycrystalline diamond from graphite. *Nature* **2003**, *421*, 599–600. [[CrossRef](#)]
47. Guignard, J.; Prakasam, M.; Largeteau, A. A Review of Binderless Polycrystalline Diamonds: Focus on the High-Pressure–High-Temperature Sintering Process. *Materials* **2022**, *15*, 2198. [[CrossRef](#)]
48. Sumiya, H.; Irifune, T.; Kurio, A.; Sakamoto, S.; Inoue, T. Microstructure features of polycrystalline diamond synthesized directly from graphite under static high pressure. *J. Mater. Sci.* **2004**, *39*, 445–450. [[CrossRef](#)]

49. Sumiya, H.; Irifune, T. Hardness and deformation microstructures of nano-polycrystalline diamonds synthesized from various carbons under high pressure and high temperature. *J. Mater. Res.* **2007**, *22*, 2345–2351. [[CrossRef](#)]
50. Sumiya, H.; Irifune, T. Microstructure and Mechanical Properties of High-Hardness nanopolycrystalline diamonds. *SEI Tech. Rev.* **2008**, *66*, 85–91.
51. Le Guillou, C.; Brunet, F.; Irifune, T.; Ohfuji, H.; Rouzaud, J.-N. Nanodiamond nucleation below 2273 K at 15 GPa from carbons with different structural organizations. *Carbon* **2007**, *45*, 636–648. [[CrossRef](#)]
52. Isobe, F.; Irifune, T.; Shinmei, T.; Suga, S.; Nishiyama, N.; Sumiya, H. Lowering P, T boundary for synthesis of pure nanopolycrystalline diamond. *J. Physics: Conf. Ser.* **2010**, *215*, 012136. [[CrossRef](#)]
53. Sumiya, H. Novel development of high-pressure synthetic diamonds “Ultra-hard Nano-polycrystalline Diamonds”. *SEI Tech. Rev.* **2012**, *74*, 15–23.
54. Sumiya, H. Novel superhard nanopolycrystalline materials synthesized by direct conversion sintering under high pressure and high temperature. *MRS Bull.* **2017**, *42*, 729–733. [[CrossRef](#)]
55. Sumiya, H.; Harano, K. Innovative Ultra-hard materials: Binderless nano-polycrystalline Diamond and nano-polycrystalline Cubic Boron Nitride. *SEI Tech. Rev.* **2016**, *81*, 21–26.
56. Irifune, T.; Ueda, C.; Ohshita, S.; Ohfuji, H.; Kunimoto, T.; Shinmei, T. Synthesis of nano-polycrystalline diamond from glassy carbon at pressures up to 25 GPa. *High Press. Res.* **2020**, *40*, 96–106. [[CrossRef](#)]
57. Irifune, T.; Isobe, F.; Shinmei, T. A novel large-volume Kawai-type apparatus and its application to the synthesis of sintered bodies of nano-polycrystalline diamond. *Phys. Earth Planet. Inter.* **2014**, *228*, 255–261. [[CrossRef](#)]
58. Sumiya, H.; Harano, K.; Arimoto, K.; Kagi, H.; Odake, S.; Irifune, T. Optical Characteristics of Nano-Polycrystalline Diamond Synthesized Directly from Graphite under High Pressure and High Temperature. *Jpn. J. Appl. Phys.* **2009**, *48*, 120206. [[CrossRef](#)]
59. Nano-Polycrystalline Diamond: Synthesis and applications. *High Press. Res.* **2020**, *40*.
60. Qian, J.; Pantea, C.; Voronin, G.; Zerda, T.W. Partial graphitization of diamond crystals under high-pressure and high-temperature conditions. *J. Appl. Phys.* **2001**, *90*, 1632–1637. [[CrossRef](#)]
61. Qian, J.; Pantea, C.; Huang, J.; Zerda, T.W.; Zhao, Y. Graphitization of diamond powders of different sizes at high pressure–high temperature. *Carbon* **2004**, *42*, 2691–2697. [[CrossRef](#)]
62. Zhan, G.D.; Moellendick, T.E.; Li, B.; Gooneratne, C. New ultra-strong and catalyst-free PDC cutting element technology. In Proceedings of the International Petroleum Technology Conference, Dhahran, Saudi Arabia, 13 January 2020. [[CrossRef](#)]
63. Lu, J.; Kou, Z.; Liu, T.; Yan, X.; Liu, F.; Ding, W.; Zhang, Q.; Zhang, L.; Liu, J.; He, D. Submicron binderless polycrystalline diamond sintering under ultra-high pressure. *Diam. Relat. Mater.* **2017**, *77*, 41–45. [[CrossRef](#)]
64. Liu, J.; Zhan, G.; Wang, Q.; Yan, X.; Liu, F.; Wang, P.; Lei, L.; Peng, F.; Kou, Z.; He, D. Superstrong micro-grained polycrystalline diamond compact through work hardening under high pressure. *Appl. Phys. Lett.* **2018**, *112*, 061901. [[CrossRef](#)]
65. Li, Q.; Zhan, G.; Li, D.; He, D.; Moellendick, T.E.; Gooneratne, C.P.; Alalsayednassir, A.G. Ultrastrong catalyst-free polycrystalline diamond. *Sci. Rep.* **2020**, *10*, 22020. [[CrossRef](#)]
66. He, D.; Xu, C.; Wang, H. Method for Preparing High-Performance Polycrystalline Diamond by Utilizing Hinge-Type Cubic Press. CN Patent CN103331129A, 16 September 2015.
67. Bushlya, V.; Petrusa, I.; Gutnichenko, O.; Osipov, O.; M’Saoubi, R.; Turkevich, V.; Ståhl, J.-E. Sintering of binderless cubic boron nitride and its modification by β -Si₃N₄ additive for hard machining applications. *Int. J. Refract. Met. Hard Mater.* **2020**, *86*, 105100. [[CrossRef](#)]
68. Zhao, M.; Kou, Y.; Zhang, Y.; Peng, B.; Wang, Y.; Wang, Z.; Yin, X.; Jiang, M.; Guan, S.; Zhang, J.; et al. Superhard transparent polycrystalline cubic boron nitride. *Appl. Phys. Lett.* **2021**, *118*, 151901. [[CrossRef](#)]



an Open Access Journal by MDPI

Editor-in-Chief

Prof. Dr. Maryam Tabrizian

James McGill Professor,
Professor of Biomedical
Engineering, Professor of
Bioengineering, Professor of
Experimental Surgery,
Department of Biomedical
Engineering, Faculty of
Medicine/Faculty of Dentistry,
Duff Medical Science Building,
3775 University Street, Montreal,
QC H3A 2B4, Canada

Message from the Editor-in-Chief

Materials (ISSN 1996-1944) was launched in 2008. The journal covers twenty comprehensive topics: biomaterials, energy materials, advanced composites, structure analysis and characterization, porous materials, manufacturing processes and systems, advanced nanomaterials, smart materials, thin films and interfaces, catalytic materials and carbon materials, materials chemistry, materials physics, optics and photonics, corrosion and materials degradation, construction and building materials, materials simulation and design, electronic materials, advanced and functional ceramics, metals and alloys, general. The distinguished and dedicated editorial board and our strict peer-review process ensure the highest degree of scientific rigor and review of all published articles. *Materials* provides a unique opportunity to contribute high quality articles and to take advantage of its large readership.

Author Benefits

Open Access:— free for readers, with [article processing charges \(APC\)](#) paid by authors or their institutions.

High Visibility: indexed within [Scopus](#), [SCIE \(Web of Science\)](#), [PubMed](#), [PMC](#), [Ei Compindex](#), [CaPlus / SciFinder](#), [Inspec](#), [Astrophysics Data System](#), and other databases.

Journal Rank: [JCR](#) - Q1 (*Metallurgy & Metallurgical Engineering*) / [CiteScore](#) - Q2 (*Condensed Matter Physics*)

Contact Us

Materials
MDPI, St. Alban-Anlage 66
4052 Basel, Switzerland

Tel: +41 61 683 77 34
www.mdpi.com

mdpi.com/journal/materials
materials@mdpi.com
[@Materials_Mdpi](#)